Climent, H.; Dolz, V.; Pla Moreno, B.; González-Domínguez, D. (2022). Analysis on the potential of EGR strategy to reduce fuel consumption in hybrid powertrains based on advanced gasoline engines under simulated driving cycle conditions. Energy Conversion and Management. 266:1-15. https://doi.org/10.1016/j.enconman.2022.115830

Analysis on the potential of EGR strategy to reduce fuel consumption in hybrid powertrains based on advanced gasoline engines under simulated driving cycle conditions

Héctor Climent, Vicente Dolz, Benjamín Pla, David González-Domínguez*

CMT Motores Térmicos, Universitat Politècnica de València, Spain

*Corresponding author: dagondo1@mot.upv.es. Telephone: (+34) 96 387 76 50. Postal address: CMT-Motores Térmicos. Universitat Politècnica de València. Camino de Vera s/n. 46022. Valencia. Spain.

Highlights

- EGR impact on the fuel economy of SI engines evaluated through vehicle simulations.
- Conventional and hybrid vehicles simulated during WLTP driving cycles.
- EGR leads to a fuel consumption reduction of 2.6% in conventional cars.
- Hybridization increases the EGR benefit in fuel economy up to 4.6%.

Keywords

EGR, gasoline engine, fuel economy, hybrid electric vehicle, WLTP cycle simulation

Abstract

The increased concern for environmental problems has boosted the electrification of passenger cars to remove air pollutant emissions from urban areas. Automotive manufacturers have predominantly opted for hybrid powertrains with advanced gasoline engines, because of the current limitations of battery electric vehicles and the higher costs of diesel aftertreatment systems. Meanwhile, the exhaust gas recirculation (EGR) strategy decreases fuel consumption and CO_2 emissions in gasoline engines. The powertrain hybridization may increase the EGR benefit in fuel consumption, given that the dependence of internal combustion engine (ICE) operation on the driver's power demand is reduced. The ICE can usually operate at medium loads, around its maximum efficiency zone, where the EGR benefit is greater than at low loads. Therefore, this research aimed to quantify the fuel saving achieved with EGR in a gasoline-electric hybrid powertrain under driving cycle conditions. To this end, vehicle 0D simulations were performed using a map-based engine fuel consumption model. Engine tests and 1D simulations were carried out to obtain ICE fuel maps with and without EGR. Besides, the transient performance of the vehicle 0D model was validated with experimental data. Both rule- and optimization-based strategies were used to manage the power split between the engine and electric motor. Modeling results revealed that EGR improves fuel economy by 4.6% in the hybrid powertrain during a WLTP class 3b driving cycle, 2% more than in the conventional one.

Acronyms

AMF	air mass flow
BEV	battery electric vehicle
BMEP	brake mean effective pressure
BSFC	brake specific fuel consumption
DOE	design of experiments
ECMS	equivalent consumption minimization strategy
ECU	engine control unit
EGR	exhaust gas recirculation
EM	electric motor
EMS	energy management system
FSM	finite-state machine
HEV	hybrid electric vehicle
ICE	internal combustion engine
IMEP	indicated mean effective pressure
RB	rule-based
SI	spark ignition
SOC	state of charge
SUV	sport utility vehicle
TWC	three-way catalyst
VVT	variable valve timing
WLTP	Worldwide harmonized Light vehicle Test Procedure

1. Introduction

The strong commitment of many national governments with the fight against climate change is promoting new environmental policies to reduce greenhouse gas emissions. As an example of this, the European Commission has recently projected a reduction of 50% in the CO_2 emissions for new passenger cars by 2030 [**1**], as compared to the 2021 target (95 gCO_2/km). This scenario is forcing automotive manufacturers to opt for electrified powertrains in search of greener technologies. Battery electric vehicles (BEVs) are the strongest alternative without fossil fuels, but they have critical limitations at present, such as lower power densities and higher production costs than conventional cars, long recharge times, and short driving ranges. Besides, BEV's benefit in the well-to-wheel CO_2 emissions is challenging to quantify and may vanish depending on the energy mix [**2**, **3**]. Under such circumstances, hybrid-electric powertrains usually based on advanced spark-ignition (SI) engines (commonly fueled with gasoline) have been positioned as the most attractive solution for passenger cars in the upcoming years.

Some recent research studies have evidenced the capability of hybridization to enhance fuel economy in passenger cars [**4**, **5**]. Asghar et al. [**6**] and García et al. [**7**] evaluated via modeling the performance of innovative SI engines working in parallel hybrid electric vehicles (HEVs). They revealed that HEVs saved up to 12% and 17% fuel as compared to the equivalent non-hybrid architecture, during a standard Manhattan driving cycle and a Worldwide harmonized Light vehicle Test Procedure (WLTP) cycle, respectively. Huang et al. [**8**] tested two pairs of conventional and full-hybrid gasoline vehicles on three real routes by using portable emission measurement systems; and they found fuel improvements of 23-49% in favor of the hybrid concepts. The success of powertrain hybridization combined with SI engines is mainly built on the reduction of the engine operating time at low load, where pumping and friction losses are high in relative terms [**9**, **10**], and the simplicity of the three-way catalyst (TWC) compared with diesel aftertreatment systems [**11**].

Concerning the current trends in SI engines, the most common way of improving fuel efficiency is downsizing with direct fuel injection, while turbocharging is required to compensate the consequent power loss [**12**, **13**]. Lumsden et al. [**14**] and Shaded et al. [**15**] stated that downsizing along with direct injection may lead to fuel savings of up to 25%, due to the reduction in the pumping and friction losses and the increase in the compression ratio. Another interesting strategy is the exhaust gas recirculation (EGR), whose application in SI engines has been widely documented in the literature [**16**, **17**]. Luján et al. [**18**] and Siokos et al. [**19**] concluded that the use of EGR results in fuel improvements because of a reduction in the pumping and in-cylinder heat losses, combined with a better combustion phasing thanks to a lower knock tendency. In addition, EGR avoids fuel enrichment at high engine speeds and loads to control the gas temperature limitations at the turbine inlet [**20**].

The benefit of EGR in the fuel consumption of SI engines is not uniform on the whole engine operating map. The fuel improvement with EGR at medium-high loads is generally higher than at medium-low loads, mainly due to a lower EGR tolerance as the engine load is reduced [**16**, **19**]. Knowing this, the powertrain hybridization may maximize the EGR impact on fuel economy, given that the internal combustion engine (ICE) operation can be concentrated

around its maximum thermal efficiency zone, just located at medium-high loads. Hence, the main objective of this research is to assess how the powertrain hybridization affects the potential of EGR strategy to improve the fuel economy in gasoline engines. To this end, the performance of a hybrid sport utility vehicle (SUV) and its conventional counterpart was simulated for an engine operation with and without EGR during a WLTP class 3b driving cycle. These simulations were performed using GT-Power 0D models with a map-based engine fuel consumption approach. Besides, engine tests and 1D simulations were carried out to obtain the ICE fuel maps.

Regarding the type of hybridization, a parallel full hybrid electric powertrain with a battery capacity of 2 kWh is selected for the present work. HEVs are usually divided into mild, full (FHEV) and plug-in (PHEV), in ascending order of electrification, based on the battery size and charge source [**21**]. Although PHEV seems to be the most promising solution to comply with the CO2 emission reduction objectives [**22**], FHEV is currently the most attractive technology for automotive manufacturers owing to its lower complexity and costs, and good results in terms of fuel economy [**23**]. HEVs can be also classified into three groups according to the powertrain layout: series, parallel (P2) and series-parallel. The major advantage of parallel architecture is that the electric motor is smaller than in the series layout, and the generator is not required. By contrast, the engine speed in the parallel hybrids cannot be freely set, unlike in the series ones. Series-parallel architecture combines the strengths of series and parallel layouts, improving the fuel economy, but its application involves additional complexity and costs. At present, the parallel configuration is the most competitive due to its simplicity, lower expense in electrical components, and similar fuel consumption to more complex solutions [**7**, **24**].

The paper is organized into three sections: the engine test cell and 1D model, SUV 0D models and methods are described in Section 2; the results and discussion are presented in Section 3; and the main conclusions are given in Section 4.

2. Materials and methods

A series of inputs are required to perform conventional and hybrid SUV 0D simulations, such as engine fuel and emission maps, vehicle aerodynamics and geometry and electrical components' specifications. To determine the engine maps, 16 steady-state working points are selected to cover the bulk of the engine operation without EGR during a WLTP cycle previously tested in the engine test cell. Engine tests and 1D simulations are then used to optimize these 16 operating points with EGR. In the case of the hybrid powertrain, an energy management strategy (EMS) is also required to define the power split between the internal combustion engine (ICE) and electric motor. Both rule-based control and equivalent consumption minimization strategies are utilized in this research. Hence this section is divided into five parts: (2.1) engine test cell, (2.2) engine 1D model, (2.3) obtention of optimized engine maps, (2.4) SUV 0D models, and (2.5) energy management strategies.

2.1. Engine test cell

In this work, the same experimental facility and instrumentation as in a previous study [**25**] is used. A downsized (1.3l) turbocharged direct injection SI gasoline engine is employed, and its principal attributes are summarized in **Table 1**. The engine also includes the following technologies: four-way catalyst (FWC), variable valve timing (VVT) and variable nozzle turbine. The FWC integrates the functionality of a conventional TWC with a gasoline particulate filter into a single device. The VVT system allows advancing or delaying the camshaft timing in a range of 40 degrees for both intake and exhaust sides, while keeping constant the valve lift and opening duration. Besides, a low-pressure EGR loop has been added to the base engine. This is composed of an EGR valve, a water-to-air cooler and a T-shape flow splitter to extract exhaust gases downstream of the aftertreatment. A second valve is also installed in the intake line, just upstream of the EGR joint, in order to operate with high EGR levels. The schematic engine layout is given in **Figure 1**.

Table 1. Engine's attributes

Attribute	Description
Technology	SI gasoline turbocharged direct injection
Displacement	1300 cc
Compression ratio	10:1
Number of cylinders	4
Camshaft system	Variable valve timing
Total number of valves (intake/exhaust)	8/8
Turbocharger	Variable nozzle turbine
Aftertreatment system	Four-way catalyst

The engine is installed and fully instrumented in a dynamic test bench controlled with the AVL PUMA software, which regulates the engine speed and torque by using an AVL AFA 200/4-8EU dynamometric brake. The AVL PUMA software is also used to acquire the main pressure and temperature values, air and fuel mass flows, turbocharger speed and engine raw emissions, all with 20 Hz acquisition frequency. The location of the pressure (Kistler 4260A piezoresistive type transmitters) and temperature (K-type thermocouples) sensors is shown in **Figure 1**. The turbocharger speed and the air and fuel mass flows are registered with the following devices: MICRO-EPSILON DZ140, AVL FLOWSONIX and AVL 733S. In addition, a HORIBA MEXA-ONE gas analyzer is connected upstream of the FWC to measure raw NOx, CO_2, CO and HC emissions. The EGR rate is estimated from the intake and exhaust CO_2 concentrations as follows [**26**]:

$$EGR\ [\%] = \frac{[CO_2]_{intake} - [CO_2]_{ambient}}{[CO_2]_{exhaust} - [CO_2]_{ambient}} \cdot 100 \quad (1)$$

where the intake ($[CO_2]_{intake}$) and exhaust ($[CO_2]_{exhaust}$) mole fractions of CO_2 are measured at the intake manifold and turbine outlet, respectively. The $[CO_2]_{ambient}$ represents the ambient mole fraction of CO_2.

Crank-angle resolved pressure traces are measured in the manifolds by means of two Kitsler 601CAA piezoelectric type sensors, and in the four cylinders with four AVL Z133 spark plugs with integrated pressure sensors. Such instantaneous pressure signals are registered with a sampling of 0.2 crank-angle degrees, through the PXI 6123 and PXI 6251 acquisition modules programmed with Labview by National Instruments TM [**27**, **28**]. Moreover, the original engine control unit (ECU), designed for the base engine with no EGR, is partially bypassed with the ETAS ES910 prototyping and interface module to enable any variations on the throttle position, VVT system, spark timing, and injected fuel. In order to ensure a proper lambda control when operating with EGR, the ECU is also equipped with an air flowmeter at the air-filter outlet. Finally, the EGR valves and VNT position are managed by means of the PXI 7813R and NI 9759 control modules [**27**, **28**], in open-loop configuration independently from the ECU.

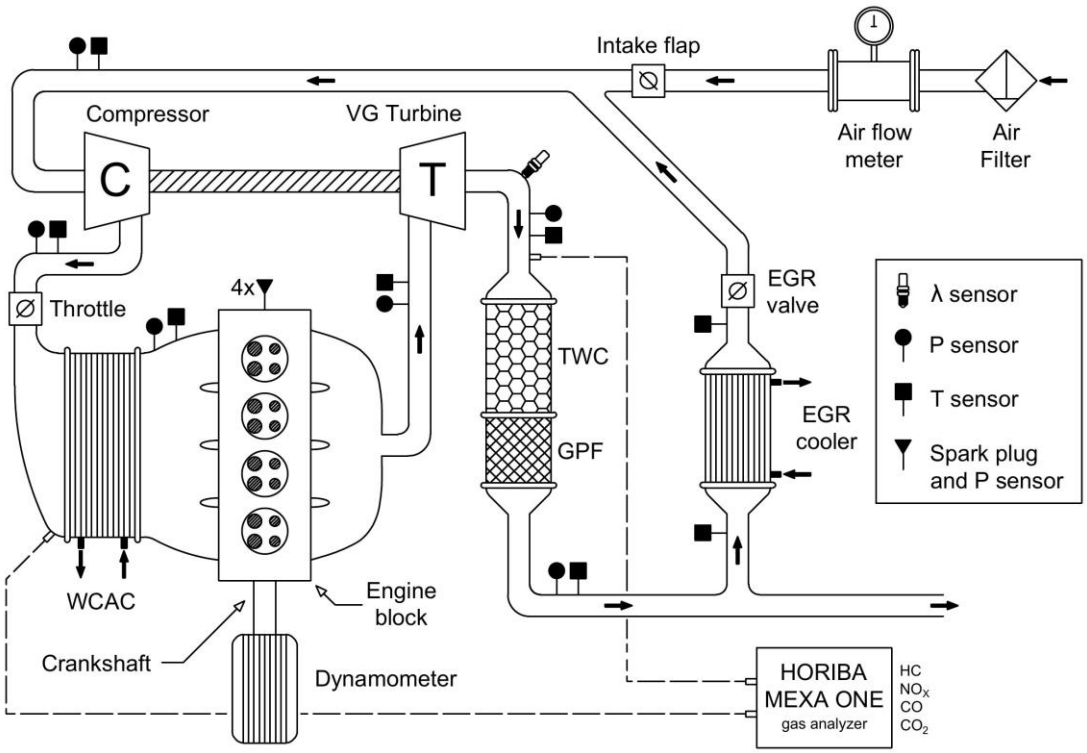

Figure 1. Schematic engine layout.

2.2. Engine 1D model

A 1D model of the whole gasoline engine described in Section 2.1 has been developed by means of the software GT-Power, including the EGR, VVT and VNT technologies. The model has been calibrated according to the procedure explained in two previous studies [**29**, **30**], using the experimental data of 16 steady-state operating points tested with different EGR rates and VVT settings. Complete information about these experiments is provided in Section 2.3. The calibration procedure consists of three stages: tuning of fitting parameters, model validation and obtention of empirical correlations. Such correlations are implemented into the model to adjust heat transfer and pressure drop phenomena in engine lines and volumes [**29**]. In the first stage, engine tests are reproduced with the 1D model to tune fitting parameters, such as heat transfer multipliers, friction multipliers and discharge coefficients. To this end, the model is set in the following way: firstly, the turbocharger is decoupled by unlinking compressor and turbine

powers to regulate the intake and exhaust manifold pressures at the same time; and secondly, a series of PI controllers is configured to modify the fitting parameters, in order to replicate the experimental cycle-averaged temperature and pressure values around the turbocharger and at the intake and exhaust manifolds.

Once the engine tests are reproduced with the model, a validation process is performed. The modeled values of the air mass flow (AMF) and indicated mean effective pressure (IMEP) are compared with their respective experimental ones. The instantaneous pressure traces in the manifolds and cylinders are also checked. In order to obtain reliable empirical correlations that assure the high quality of the model calibration, an error threshold of 5% is considered for the AMF and IMEP variables. In other words, the fitting parameters of each simulation are only utilized as inputs for the correlations if the corresponding AMF and IMEP relative errors are lower than 5%. The AMF and IMEP modeling errors related to the 16 operating points used for the model calibration are presented in Section 2.3. As a final step, some empirical correlations are determined from the validated fitting parameters. The engine 1D model also contains hot-exposed turbocharger maps formerly extrapolated and adiabatized [**31**], and an Artificial Neural Network (ANN) trained, as described in [**29**], to reproduce the combustion process through the Wiebe function [**32**]. The main attributes of the empirical correlations and ANN implemented into this model are shown in **Table 2**.

Table 2: Characteristics of the empirical correlations implemented into the model. (*) R^2 related to the ANN training data set.

Involved variable	Fitting parameter	Dependent variables	Correlation type	R^2
Intake manifold pressure	Throttle discharge coefficient	Throttle angle	Look-up table	-
Intake manifold temperature	WCAC coolant flow	Engine speed and IMEP	3D map from scattered data	-
Turbine inlet temperature	Heat transfer multiplier of exhaust manifold	Exhaust ports temperature and exhaust gases mass flow	Linear polynomial equation	0.81
Aftertreatment pressure drop	TWC pressure drop	TWC gas volume flow	Look-up table	-
Exhaust line pressure drop	Exhaust line pressure drop	Exhaust line gas volume flow	Look-up table	-
EGR cooler inlet temperature	Heat transfer multiplier of EGR line	TWC outlet temperature and EGR flow	Linear polynomial equation	0.75
EGR cooler outlet temperature	Coolant flow in the EGR cooler	Engine speed and IMEP	3D map from scattered data	-
Combustion phasing (Wiebe function)	CA50	Spark timing, AFR, engine speed and in-cylinder pressure, temperature, trapped mass and residual gas fraction at IVC.	Quadratic polynomial neural network	0.98*
Combustion duration (Wiebe function)	CA1090	Spark timing, AFR, engine speed and in-cylinder pressure, temperature, trapped mass and residual gas fraction at IVC.	Quadratic polynomial neural network	0.96*
Engine friction losses	FMEP	Engine speed and maximum cylinder pressure	Chen-Flynn model	0.81

2.3. Obtention of optimized engine maps

A WLTP class 3b driving cycle for an engine operation with no EGR was performed in the engine test cell presented in Section 2.1, by considering the characteristics (aerodynamics, geometry, transmission, tires, etc.) of the conventional SUV selected for this research. These vehicle attributes are described in Section 2.4. **Figure 2** shows the WLTP speed profile for class 3b vehicles (a) and the experimental ICE operating points recorded with a sampling frequency of 10 Hz during the driving cycle (b).

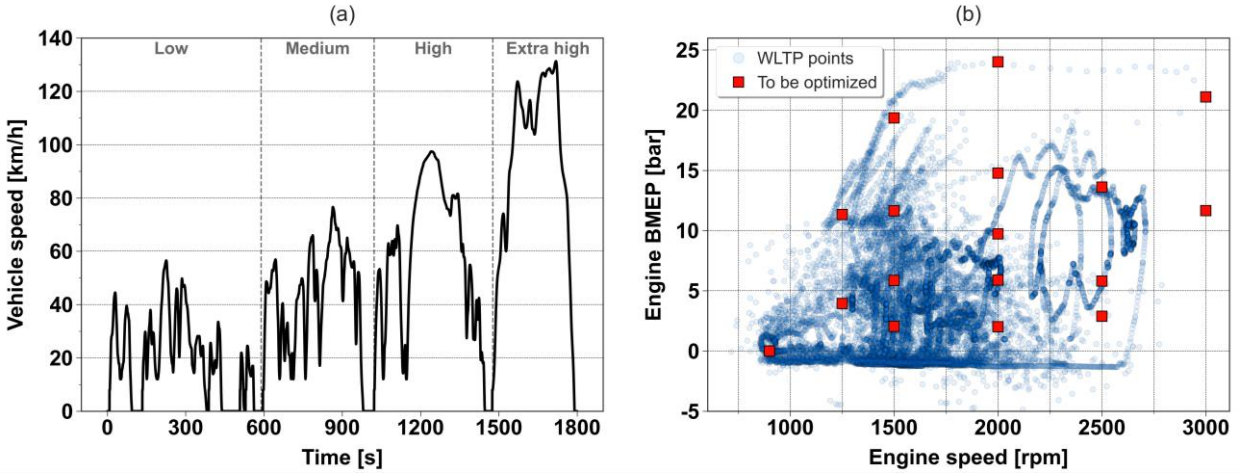

Figure 2. WLTP speed profile for class 3b vehicles (a) and experimental ICE operating points during the WLTP class 3b driving cycle (b). The 16 operating points to be optimized with EGR and the idle conditions at 900 rpm marked with red squares in (b).

Given that the ECU was developed for the original engine without EGR, the ICE performance with EGR had to be optimized. To this end, 16 steady-state working points were chosen to cover most of the engine operation. The EGR rate, VVT settings and spark timing of these 16 points were optimized to improve fuel economy, by following the method designed in a previous study [**30**] to reduce the workload and costs in the engine test bench. The 16 engine operating points to be optimized with EGR and the engine idle conditions at 900 rpm (with no EGR) are also shown in **Figure 2**b (red squares).

The optimization of the mentioned 16 operating points is composed of three stages: experimental EGR sweeps for three pairs of VVT settings to calibrate the engine 1D model, a design of experiments (DOE) by simulation to find the optimum EGR and VVT values, and a reduced experimental DOE to verify the trends observed by means of the model. Accordingly, around 300 experiments were performed firstly, in which six EGR rates (0, 5, 10, 15, 20 and 25%) at the minimum, intermediate and maximum valve overlap conditions were tested for each of the 16 operating points. The spark timing was fixed in every test considering that the optimal combustion start in gasoline engines usually results in a value of CA50 (crank-angle degree at 50% heat release) from 5 to 10 crank-angle degrees after top dead center [**33**]. The CA50 value is calculated in the engine test cell in real time using the apparent heat release (HR), as detailed in [**28**]. The apparent HR is the estimation of the heat released by the fuel ignoring heat transfer from the combustion chamber to walls. Besides, the ratio of the specific heats is replaced by a constant parameter (κ) which is usually around 1.3. In this way, the apparent HR can be easily

calculated just with the instantaneous in-cylinder pressure and volume. **Eq. (2)** presents the first law of thermodynamics for the combustion chamber assuming ideal gas behavior, while **Eq. (3)** provides the apparent heat release rate (AHRR).

$$\frac{dQ_f}{dt} = \frac{c_p}{c_p - c_v} p_{cc} \frac{dV_{cc}}{dt} + \frac{c_v}{c_p - c_v} V_{cc} \frac{dp_{cc}}{dt} + \frac{dQ_w}{dt} \quad (2)$$

$$AHRR = \frac{\kappa}{\kappa - 1} p_{cc} \frac{dV_{cc}}{dt} + \frac{\kappa}{\kappa - 1} V_{cc} \frac{dp_{cc}}{dt} \quad (3)$$

where p_{cc} and V_{cc} are the instantaneous pressure and volume at the combustion chamber, Q_f is the heat released by the fuel, Q_w is the heat transfer from the combustion chamber to walls, and the terms c_p and c_v represent the specific heats at constant pressure and volume, respectively.

Later on, the 300 experiments were replicated in the engine 1D model for its calibration. The model calibration methodology, concisely described in Section 2.2, is explained in detail in a previous study [**29**]. The AMF and IMEP modeling errors related to these 300 cases are shown in **Figure 3** and **Figure 4**. More specifically, three types of errors were calculated for every operating point, comparing the actual and predicted values of both variables: mean percentage error (MPE), mean absolute percentage error (MAPE) and maximum error (in absolute value). The MPE is a functional indicator to evaluate the calibration procedure, because MPE values around 0% involve that making additional efforts to tune fitting parameters is useless. Finally, it should be remarked that all AMF and IMEP maximum errors are inside the 5% threshold defined in Section 2.2.

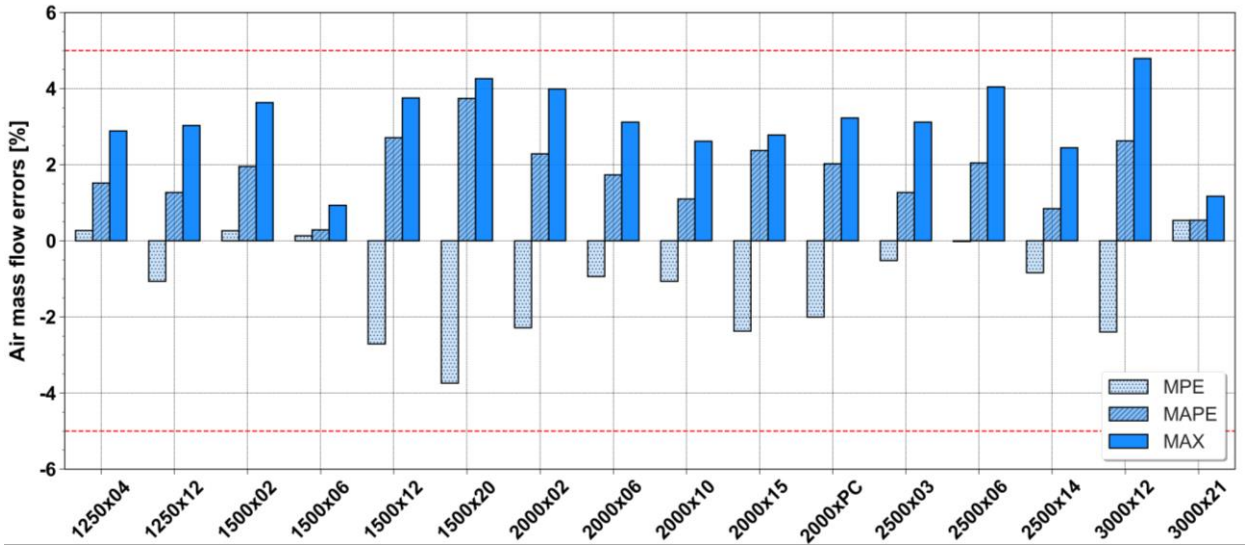

Figure 3: Modeling errors in terms of AMF related to the 16 operating points used for the engine 1D model calibration. In the x-axis labels, the first value is referred to the engine speed (rpm) and the second one to the engine BMEP (bar).

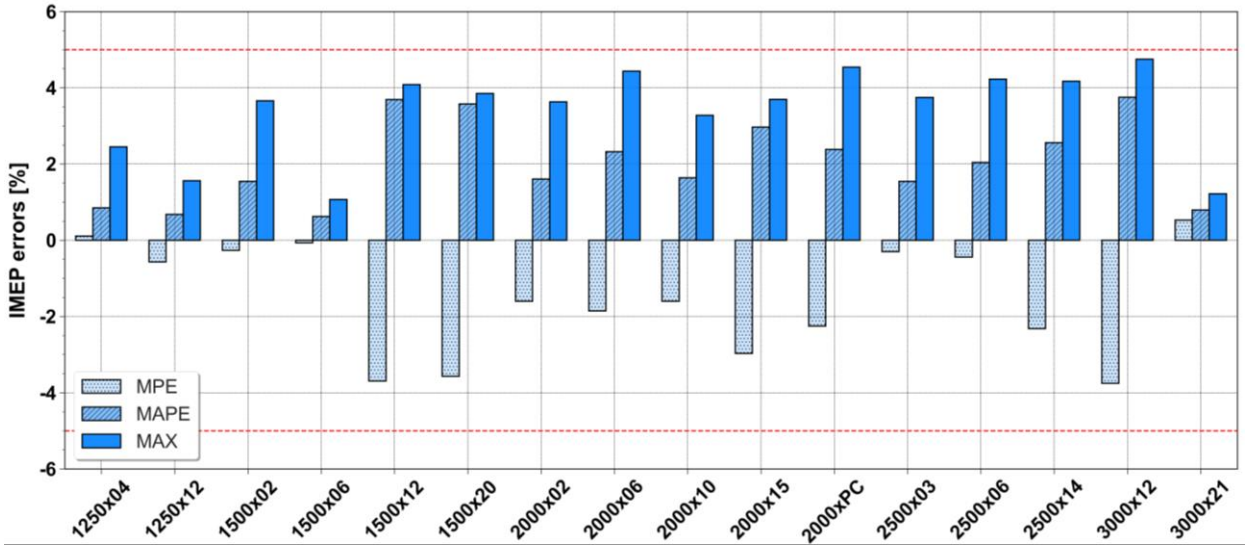

Figure 4: Modeling errors in terms of IMEP related to the 16 operating points used for the engine 1D model calibration. In the x-axis labels, the first value is referred to the engine speed (rpm) and the second one to the engine BMEP (bar).

Once the model was calibrated, a DOE with 150 simulations per operating point was carried out. Twenty-five pairs of VVT settings were considered for the same six EGR rates (0, 5, 10, 15, 20 and 25%). **Figure 5** presents an example of the modeling results obtained by means of this DOE at 3000 rpm and 12 bar BMEP: (a) contour map of indicated efficiency as a function of intake and exhaust VVT parameters for 20% EGR, and (b) the evolution of indicated efficiency for different EGR rates at minimum, maximum and optimum valve overlap conditions. Regarding **Figure 5**a, the combinations of intake valve opening (x-axis) and exhaust valve closing (y-axis) equal to 0-0 and 40-40 provide the minimum and maximum valve overlap, respectively. Finally, a reduced DOE with 10 experiments per operating point was performed to complete the optimization, in which the best combinations of EGR and VVT values in terms of fuel efficiency found via modeling were tested [**30**].

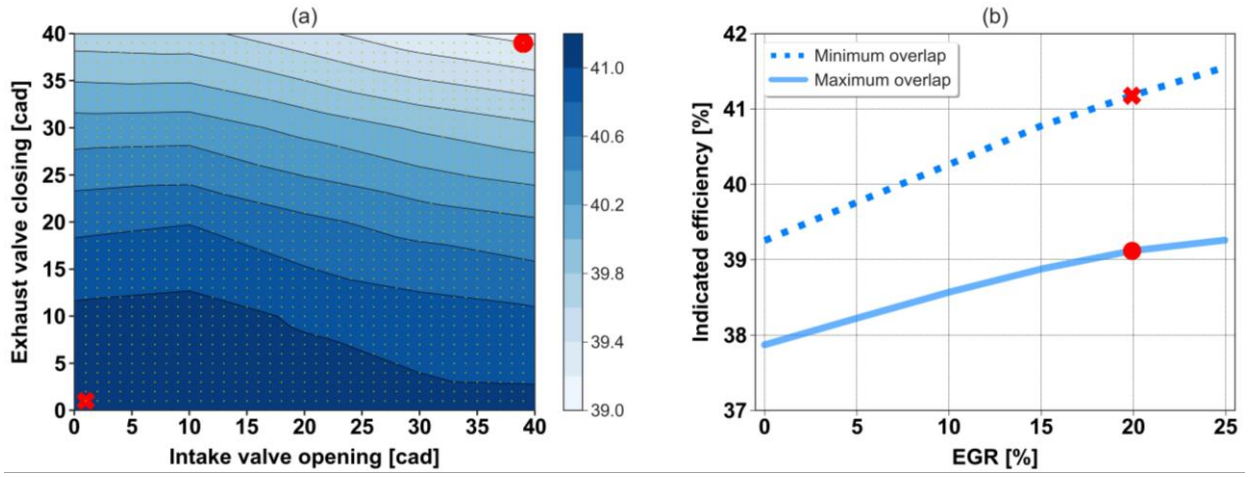

Figure 5: Optimization of engine operation with EGR at 3000 rpm and 12 bar BMEP: (a) contour map of indicated efficiency as a function of intake and exhaust VVT parameters for 20% EGR, and (b) evolution of indicated efficiency for different EGR rates at minimum and maximum valve overlap conditions.

Figure 6a presents the fuel consumption map of the SI engine operating without EGR. The map was determined by interpolating the experimental data of the selected 16 working points and the idle conditions (**Figure 2**b), for which the original ECU calibration was used to define spark timing and VVT settings. Moreover, **Figure 6**b depicts the map of EGR benefit in the fuel economy. This second map was obtained by interpolating the difference in the fuel consumption between the 16 points without EGR (**Figure 6**a) and the same points optimized with EGR. The black dashed line on both maps represents the minimum brake specific fuel consumption (BSFC) curve for each engine speed. The maximum EGR benefits are located at engine medium loads, with a peak of 6% at 15 bar BMEP and 2000 rpm (**Figure 6**b). Significant fuel improvements are also found at high loads and 3000 rpm, while very limited fuel savings are achieved with EGR at low loads. The fuel consumption reduction achieved with EGR for each operating point is provided in **Figure 7**.

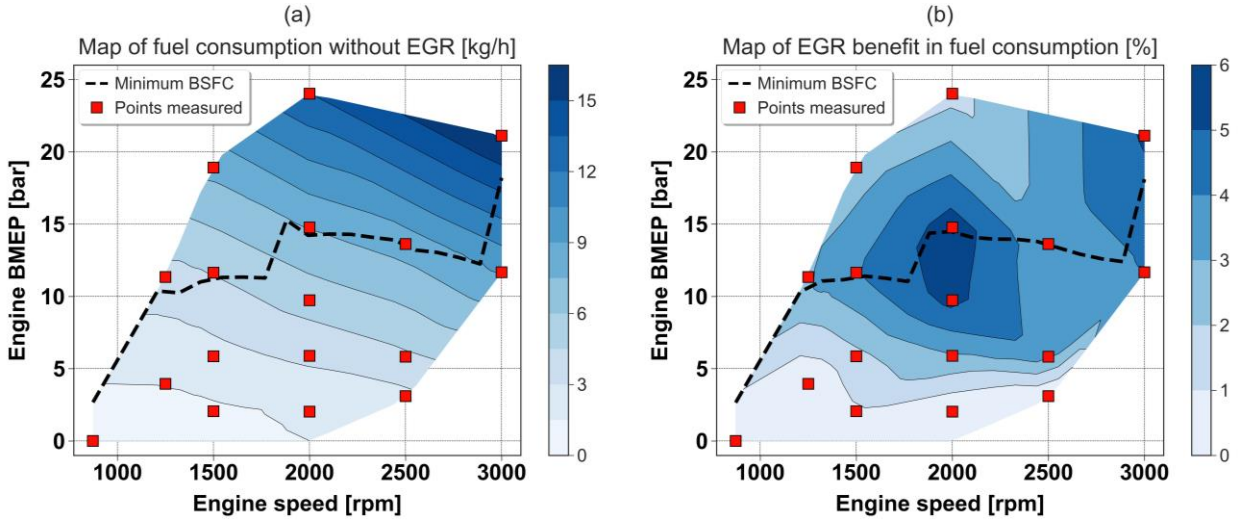

Figure 6. Contour map of fuel consumption (kg/h) for ICE operation with no EGR (a), and contour map of EGR benefit (%) in fuel economy (b). The operating points measured to obtain the maps are represented with red squares, and the minimum BSFC curve with the black dashed line.

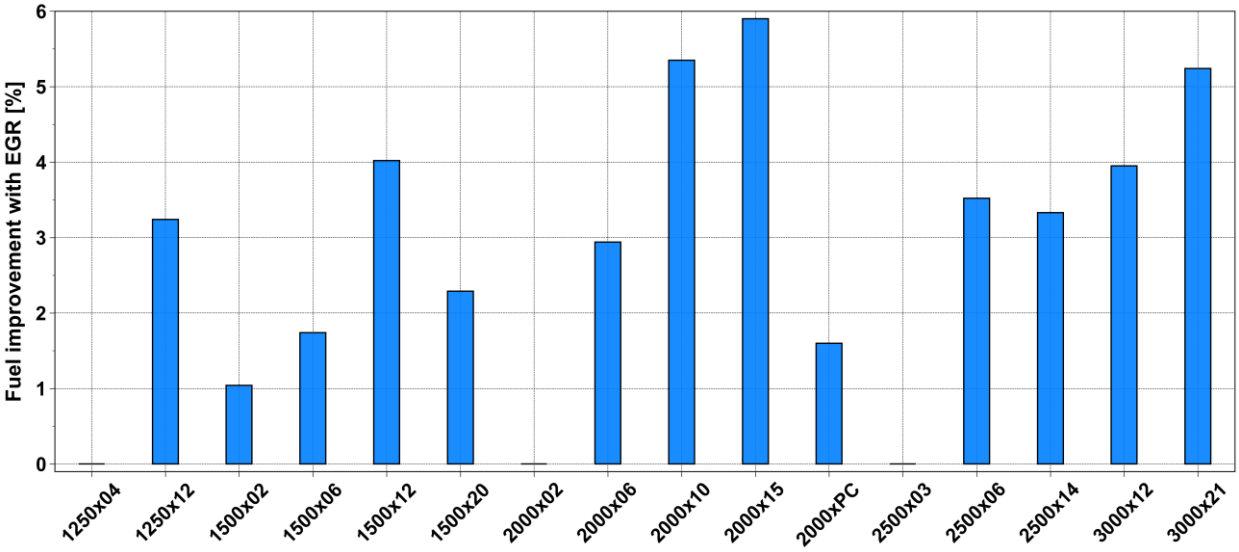

Figure 7: Improvement in fuel economy achieved with EGR for the 16 operating points selected to obtain the ICE maps. In the x-axis labels, the first value is referred to the engine speed (rpm) and the second one to the engine BMEP.

2.4. SUV 0D models

2.4.1. Conventional vehicle model

The passenger car selected to perform WLTP driving cycle simulations is a real conventional sport utility vehicle of 2018, equipped with the 160 hp gasoline engine described in Section 2.1. A 0D model of this SUV was developed by means of GT-Power. The conventional SUV model consists of five subassemblies, named as 'ICE', 'ECU', 'Driver controller', 'Gearbox' and 'Vehicle', as shown in the schematic model layout in **Figure 8**. The sub-model 'ICE' is responsible for the estimation of engine fuel consumption and emissions using the experimental data of the selected 16 operating points. This sub-model also requires other inputs, such as the engine geometry, fuel properties, power demand and fuel injection shut-off strategy. The latter is defined in the part 'ECU', a basic finite-state machine. The fuel is shut off during braking events, if torque demand is negative and lower than the negative of engine friction torque, and during gear shifts.

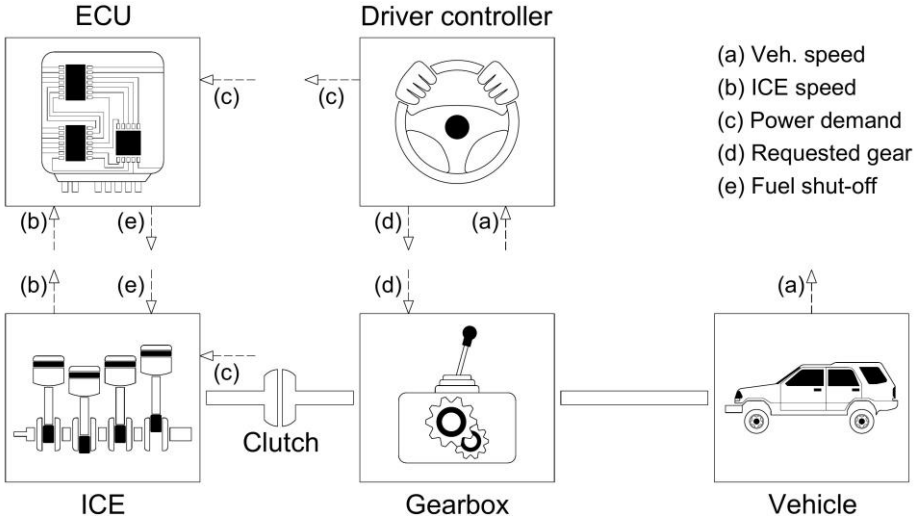

Figure 8. Schematic layout of the conventional vehicle model.

The part 'Driver controller' is a model-based controller used to regulate the vehicle speed in dynamic simulations. This sub-model calculates a reference engine torque demand (T_{ref}) as the sum of the external forces (aerodynamics, rolling resistance and gravity), the inertia torque of the entire driveline and vehicle, and the load induced by a transient gear ratio [**34**]:

$$T_{ref} = \left[\frac{F_{ae} + F_{rr} + F_g}{R_d R_t}\right] r_w + \left[I_{it} + \frac{I_{ot}}{R_t^2} + \frac{I_d}{R_t^2} + \frac{I_a}{R_d^2 R_t^2} + \frac{M_v r_w^2}{R_d^2 R_t^2}\right] \dot{\omega}_d + \left[\frac{I_{ot}}{R_t^3} + \frac{I_d}{R_t^3} + \frac{I_a}{R_d^2 R_t^3} + \frac{M_v r_w^2}{R_d^2 R_t^3}\right] \omega_d \dot{R}_t \quad (4)$$

where F_{ae}, F_{rr} and F_g are referred to aerodynamic, rolling resistance and gravity forces. The differential ratio, transmission ratio and wheel radius are represented by the terms R_d, R_t and r_w, respectively. The inertia moments of the input and output side transmission, driveshaft and axles are symbolized by I_{it}, I_{ot}, I_d and I_a; while M_v and ω_d are the vehicle mass and driveline speed on the clutch output side. Once the reference torque demand is calculated, it is corrected by a PI controller to minimize the error between the actual and desired vehicle speed [**34**]. As a

function of ICE speed, a gear shift strategy is also specified in the 'Driver controller' to manage the gearbox. Finally, the vehicle aerodynamics and geometry, together with the transmission characteristics, are defined in the subassemblies 'Vehicle' and 'Gearbox'. The main specifications of the selected conventional SUV, provided in the manufacturer's website, are shown in **Table 3**.

Table 3. SUV specifications.

Attribute	Description
Vehicle, passenger and cargo mass	1500 kg
Vehicle drag coefficient	0.33
Frontal area	2.38 m^2
Tires	215/60 R17
Gearbox	6-speed manual
Gear ratios	4.35, 2.48, 1.55, 1.14, 0.89 and 0.75
Differential ratio	3.6

2.4.2. Parallel FHEV model

A parallel in-line full hybrid powertrain with a 2-kWh battery package was selected for this research. The schematic layout of the hybrid SUV model, also created in GT-Power, is attached in **Figure 9**. The main differences between this hybrid vehicle 0D model and its conventional counterpart, described in Section 2.4.1, are the integration of the battery, a 50 kW electric motor (EM) and a second clutch (tagged as 'Clutch 1' in **Figure 9**); and the use of an EMS to determine the power split between the ICE and EM. In order to estimate the state of charge (SOC) in the battery, a simplified SOC model based on Kirchhoff's voltage law (**Eq.** (**5**)) and Coulomb Counting method (**Eq.** (**6**)) is applied:

$$R_{int} \cdot i^2 + v_{OC} \cdot i + P_b \cdot \eta_c = 0 \tag{5}$$

$$SOC_1 = SOC_0 - \frac{1}{BC}\int_{t0}^{t1} i\, dt \tag{6}$$

where the terms R_{int}, v_{OC}, i, P_b and BC are referred to the following battery parameters: internal resistance, open circuit voltage, instantaneous current, power (negative sign during battery charging) and total capacity, in that order. The Coulomb efficiency is represented by the term η_c. Besides, it should be remarked that the weight of electrical components was added to the vehicle mass, by considering 10 kg per battery capacity unit (kWh), 0.7 kg per electric motor power unit (kW) and 20 kg for the additional control units and cabling [**5**].

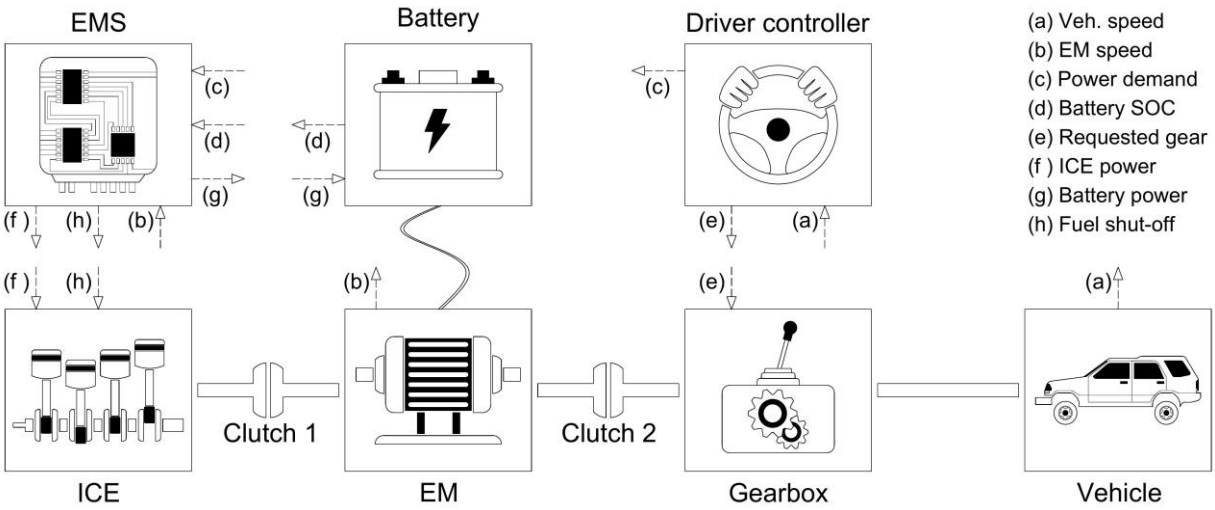

Figure 9. Schematic layout of the parallel in-line FHEV model.

2.5. Energy management strategies

Energy management strategies are required to extract the full potential of the powertrain hybridization. The main role of EMS is to find the power split between the ICE and EM that maximizes fuel economy, while supplying the driver power demand and keeping the battery SOC within a specific interval [**35**]. Energy management strategies are usually divided into two broad categories: rule-based and optimization-based methods [**36, 37**]. A deterministic rule-based EMS and a mixed EMS have been used in this research. The mixed EMS consists of an equivalent consumption minimization strategy constrained by a rule-based control to avoid the battery operation outside its usable SOC window. Both methods are described in detail below.

2.5.1. Rule-based EMS

The deterministic rule-based EMS is widely utilized by automotive manufacturers, despite not providing an optimized solution, because of its simplicity and robustness [**36**]. This strategy is implemented into the hybrid SUV 0D model by means of a GT-Power finite-state machine (FSM), which consists of states and transitions. The states are the hybrid powertrain operation modes, while the transitions are logical rules under which the FSM can shift from one state to another [**34**]. In this research, the following P2 FHEV operation modes are distinguished according to the power split between the ICE and EM: pure electric, ICE start, hybrid, conventional, regenerative braking, and conventional braking. In addition, conditional logic statements are defined for the transition between modes, based on the battery SOC, driver power demand and vehicle speed. The most important information about the operation modes is given in **Table 4**, including the ICE and EM torque demand, the state of the 'Clutch 1' (**Figure 9**) and the conditions to stay in each mode.

Table 4. Rule-based EMS: operation modes of the parallel in-line full hybrid electric vehicle.

Operation mode	ICE torque request	EM torque request	Clutch 1	Conditions
Pure electric	0	T_d	open	$SOC > SOC_{min}$ **and** $V < V_{lim}^{up}$
ICE start	0	$T_d + F_{ICE}$	closing	$\{SOC < SOC_{min}$ **or** $V > V_{lim}^{up}\}$ **and** $S_{c1} > 10$
Hybrid	T_{ICE}^*	$T_d - T_{ICE}^*$	closed	$V > V_{lim}^{low}$ **and** $S_{c1} < 10$ **and** $\{\{T_{ICE}^* \geq T_d$ **and** $SOC < SOC_{max}\}$ **or** $\{T_{ICE}^* < T_d$ **and** $SOC > SOC_{min}\}\}$
Conventional	T_d	0	closed	$V > V_{lim}^{low}$ **and** $S_{c1} < 10$ **and** $\{\{T_{ICE}^* \geq T_d$ **and** $SOC > SOC_{max}\}$ **or** $\{T_{ICE}^* < T_d$ **and** $SOC < SOC_{min}\}\}$
Regenerative braking	0	$T_d + F_{ICE}$	closed	$T_d < -F_{ICE}$ **and** $SOC < SOC_{max}$
Braking	0	0	closed	$T_d < -F_{ICE}$ **and** $SOC > SOC_{max}$

$\mathbf{T_d}$: driver torque demand; $\mathbf{T_{ICE}^*}$: ICE torque with minimum BSFC at given ICE speed; $\mathbf{F_{ICE}}$: engine friction torque; $\mathbf{V}$: vehicle speed; $\mathbf{V_{lim}^{up}}$, $\mathbf{V_{lim}^{low}}$: upper and lower limit of the vehicle speed; $\mathbf{S_{c1}}$: slip of 'Clutch 1', difference between the clutch output and input speeds.

The vehicle is initially launched at pure electric mode (unless the battery is low), that is, the EM supplies the whole driver power demand. Once either the battery is discharged or the vehicle speed is higher than a certain threshold, the ICE is started and the 'Clutch 1' is closed. While the hybrid mode is active, the engine constantly operates at its minimum BSFC curve (**Figure 6**). Therefore, the battery is always charging when the torque demand (T_d) is lower than the engine torque of minimum BSFC at a given engine speed (T_{ICE}^*), and vice versa (**Table 4**). Regarding the conventional mode, in which the vehicle is exclusively powered by the ICE, it is used under the following two scenarios: either if T_d is lower than T_{ICE}^* and the battery is totally charged, or if T_d is higher than T_{ICE}^* and the battery SOC reaches its minimum. The last two operation modes, regenerative and conventional braking, are activated when the driver torque demand is negative. During a regenerative braking, part of the vehicle kinetic energy is converted into electric energy and stored in the battery as long as the SOC is lower than its maximum. Otherwise, a conventional braking takes place. Finally, it should be mentioned that the conditions in **Table 4** related to the vehicle speed and battery SOC were optimized via DOE for the WLTP homologation cycle, as explained in Section 3.3.1.

2.5.2. Mixed EMS

Equivalent consumption minimization strategy (ECMS) proposes to address the power split problem as an instantaneous optimization problem, in which a representative cost function is minimized at each time step [**38**]. This cost function is formulated as the sum of the ICE fuel consumption, the battery power weighted through an equivalence factor and, sometimes, other terms related to harmful tailpipe emissions or drivability. The application of ECMS on hybrid powertrains has been widely studied over the last two decades, because it can be used for real-time control while achieving near-optimal results [**39**, **40**, **41**]. In this research, an ECMS with a constant equivalence factor is combined with a deterministic rule-based control (similar to the one used in the rule-based EMS), resulting in a mixed EMS. Basically, the optimum power split is calculated by means of the ECMS, and then the rule-based control determines if that optimum is feasible, to guarantee that the battery SOC is maintained within its usable window [**42**].

The ECMS is implemented into a simple Simulink model through a MATLAB function, while the rule-based control is directly built in GT-Power by using a finite-state machine, as stated in Section 2.5.1. Besides, a GT-Power interface called Simulink Harness is configured to exchange data between both models. To calculate the optimal power split, the Simulink ECMS model requires some information from the GT-Power hybrid SUV model about the powertrain state, such as: driveshaft speed (ω_d), torque demand (T_d), battery SOC and 'Clutch 1' position. The optimal power split at the time t_k is given by the ICE torque that minimizes the equivalent cost function H presented in **Eq.** (7), and that satisfies the constraints in **Eq.** (8):

$$H = Q_{LHV} \cdot \dot{m}_f(\omega_d, T_{ICE}, t_k) + \lambda \cdot P_b(\omega_d, T_d, T_{ICE}, t_k) + \gamma \cdot \left| u(T_{ICE}, t_k) - u(T_{ICE}, t_{k-1}) \right| \quad (7)$$

$$\begin{cases} T_{ICE} \leq T_{ICE,max}(\omega_d) \\ P_b \leq P_{b,max}(SOC) \end{cases} \quad (8)$$

where Q_{LHV} is the fuel lower heating value (kJ/g) and $\dot{m}_f$ is referred to the instantaneous engine fuel consumption (g/s), the latter defined by the ω_d and ICE torque (T_{ICE}). The second term $\lambda \cdot P_b$ quantifies the equivalent cost of the instantaneous battery energy consumption. The battery power P_b (kW) depends on the ω_d and electric motor torque ($T_d - T_{ICE}$), and the equivalence factor λ is a constant calibrated to achieve zero net battery energy consumption; that is, the battery is used as an energy buffer, so the ending SOC must be equal to its initial value. For the λ calibration, it was assumed that the equivalence factor for a parallel HEV is bounded on the interval defined below [**43**]:

$$1 \leq \lambda \leq \frac{\bar{\eta}_b \bar{\eta}_{EM}}{\bar{\eta}_{ICE}} \quad (9)$$

where the terms $\bar{\eta}_{ICE}$, $\bar{\eta}_{EM}$ and $\bar{\eta}_b$ are referred to the averaged efficiency of the engine, electric motor and battery, respectively.

Regarding the third term in **Eq.** (7), $\gamma \cdot |u_k - u_{k-1}|$ represents the cost associated with the additional engine fuel consumed during start and warm-up maneuvers. This last term aims at avoiding successive engine starts and shutdowns. The binary variable u is referred to the state of the 'Clutch 1' (**Figure 9**), equal to 0 if disengaged ($T_{ICE} = 0$) and 1 if engaged ($T_{ICE} > 0$), and the factor γ (kW) is a constant tuned to limit the number of starts and shutdowns. The **Eq.** (10) was used as a starting point to find the value of γ:

$$\gamma_0 = \frac{m_f^* \cdot N_{starts}}{t_{ICE}} \quad (10)$$

where γ_0 is the initial value of the factor γ, and N_{starts} the desired number of engine starts. The term t_{ICE} is referred to the total ICE operation time (s) throughout the WLTP cycle, while m_f^* represents the additional fuel consumption (g) during engine starts. A m_f^* value of 2.6 g was considered for this research. This value was estimated as the difference between the ICE fuel consumed in a start maneuver up to the idle conditions, performed in the engine test bench (Section 2.1), and the fuel consumption at steady-state idle conditions.

Given that the ECMS is integrated into a mixed EMS, the instantaneous optimal power split, or in this case the optimal ICE torque (T_{opt}), is not directly applied on the powertrain.

Instead, the T_{opt} is used as an input for a rule-based control, implemented in the GT-Power hybrid SUV model, in which the same operation modes as in the rule-based EMS (**Table 4**) are defined. However, now the transition between the pure electric and hybrid modes depends on the T_{opt}, unless the battery SOC is over its limits. It is assumed that the battery SOC can only vary between 0.3 and 0.7, that is the usable SOC window recommended by the manufacturers for the type of hybrid powertrain architecture utilized in this study [**44**, **45**]. **Table 5** shows the parallel full HEV operation modes defined in the rule-based control of the mixed EMS along with the conditions to stay in each mode.

Table 5. Mixed EMS: operation modes of the parallel in-line full hybrid electric vehicle.

Operation mode	ICE torque request	EM torque request	Clutch 1	Conditions
Pure electric	0	T_d	open	$SOC > SOC_{min}$ **and** $T_{opt} = 0$
ICE start	0	$T_d + F_{ICE}$	closing	$\{SOC < SOC_{min}$ **or** $T_{opt} > 0\}$ **and** $S_{c1} > 10$
Hybrid	T_{opt}	$T_d - T_{opt}$	closed	$T_{opt} > 0$ **and** $S_{c1} < 10$ **and** $\{\{T_{opt} \geq T_d$ **and** $SOC < SOC_{max}\}$ **or** $\{T_{opt} < T_d$ **and** $SOC > SOC_{min}\}\}$
Conventional	T_d	0	closed	$T_{opt} > 0$ **and** $S_{c1} < 10$ **and** $\{\{T_{opt} \geq T_d$ **and** $SOC > SOC_{max}\}$ **or** $\{T_{opt} < T_d$ **and** $SOC < SOC_{min}\}\}$
Regenerative braking	0	$T_d + F_{ICE}$	closed	$T_d < -F_{ICE}$ **and** $SOC < SOC_{max}$
Braking	0	0	closed	$T_d < -F_{ICE}$ **and** $SOC > SOC_{max}$

T_d : driver torque demand; **T_{opt}** : optimal engine torque calculated by means of the ECMS; **F_{ICE}** : engine friction torque; **S_{c1}** : slip of 'Clutch 1', difference between the clutch output and input speeds.

3. Results and analysis

A series of WLTP homologation cycle 0D simulations were performed to assess the EGR benefit in the fuel economy of the SI gasoline engine coupled to the conventional powertrain and its parallel full hybrid counterpart. Regarding the hybrid technology, the calibration of the EMS from the perspective of the fuel consumption reduction was previously required. In addition, the transient performance of the vehicle 0D model was validated with experimental data to assure the reliability of the findings. Hence the simulated results have been arranged into four sub-sections: (3.1) vehicle 0D model validation, (3.2) EGR impact on the fuel economy of the conventional SUV, (3.3) optimization of the hybrid powertrain, and (3.4) EGR impact on the fuel economy of the hybrid SUV.

3.1. Vehicle model validation

In the interest of reliability, a WLTP class 3b driving cycle was simulated by considering an engine operation without EGR, to validate the transient behavior of the conventional SUV model (Section 2.4.1) in terms of fuel consumption. In this simulation, the WLTP vehicle speed demand was replicated with a root-mean-square error of 1.79%, normalized by the averaged vehicle speed. The modeled fuel consumption was compared with the experimental data from the WLTP cycle presented in Section 2.3, which was performed in the engine test cell at warm conditions. **Figure 10** shows the actual and predicted values of the cumulative engine fuel

consumption (a) and the corresponding modeling error (b) for the conventional powertrain without EGR during the WLTP driving cycle. The modeling error is calculated as the difference between the actual and predicted values divided by the total fuel consumed (1064 g).

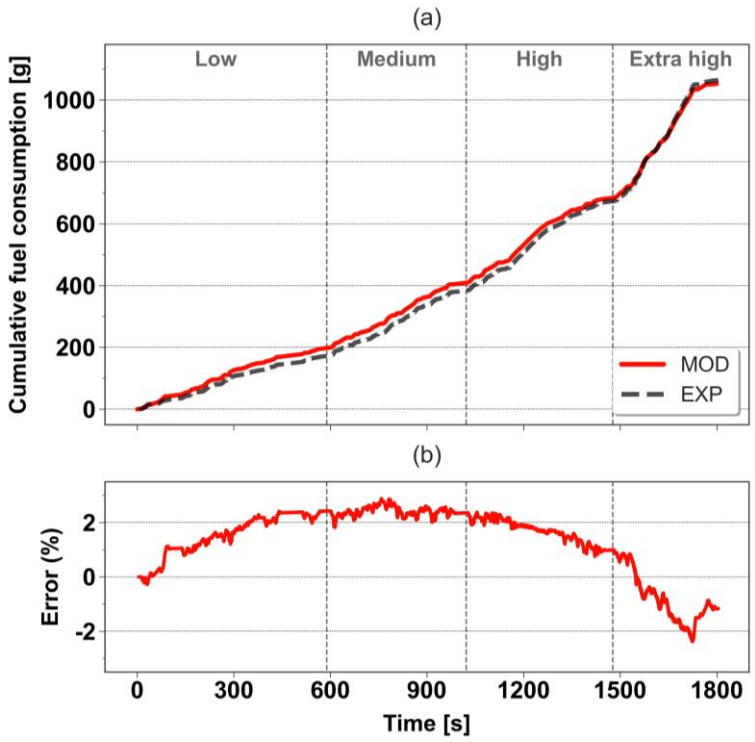

Figure 10. Actual (dashed) and predicted (solid) values of the cumulative ICE fuel consumption (a) and the corresponding modeling error (b) for the conventional SUV with no EGR during a WLTP class 3b driving cycle.

The GT-Power vehicle 0D model performance is highly accurate in terms of fuel consumption, as seen in **Figure 10b**. In the 'Low' part of the WLTP cycle, also known as urban phase, the SUV model overpredicts the fuel consumption with an accumulated error of around 2%. This discrepancy between the actual and predicted values could be explained by the lack of experimental information at very-low engine loads (**Figure 2**b). A nearly perfect model approach is observed during the 'Medium' part (suburban phase) and the first half of the 'High' part (rural phase), where the accumulated error is marginally modified. Finally, the model underpredicts the fuel consumption by more than 3% from 1200 to 1800 s. This error could be explained by the low density of experimental points at medium-high engine loads between 2500 and 3000 rpm. A negative modeling error of about 1.14% is obtained at the end of the WLTP cycle if comparing the experimental (1064 g) and modeled (1052 g) values of total fuel consumed.

3.2. EGR impact on the fuel economy of the conventional SUV

Two WLTP homologation cycles were simulated by using the conventional SUV 0D model (Section 2.4.1), to quantify the fuel economy improvement achieved because of the EGR strategy. The single difference in the vehicle model configuration between the two simulations is the maps used to reproduce the engine fuel consumption and emissions. One simulation was performed by considering an engine operation without EGR (Case A, previously presented in Section 3.1), and the other one with EGR (Case B). The bar chart in **Figure 11** shows the engine

fuel consumption in both cases at each WLTP cycle phase. The fuel saving achieved with EGR per phase, normalized by the fuel consumed without EGR at each phase, is specified just above the bars related to the case with EGR. Besides, **Figure 12** depicts the engine operating points on the contour map of EGR benefit in fuel consumption (**Figure 6**b), separately for each of the four driving cycle parts. It should be also stated that the ICE operating points required by the conventional powertrain to follow the WLTP vehicle speed demand are the same with and without EGR, and that the working points with a negative engine load are omitted in **Figure 12**.

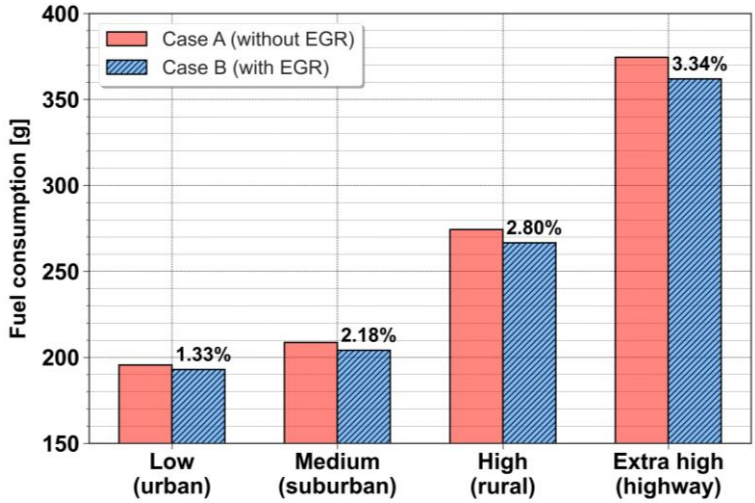

Figure 11. ICE fuel consumption without (Case A) and with (Case B) EGR for the conventional powertrain at each phase of the WLTP driving cycle. The fuel saving with EGR included above the bars related to Case B.

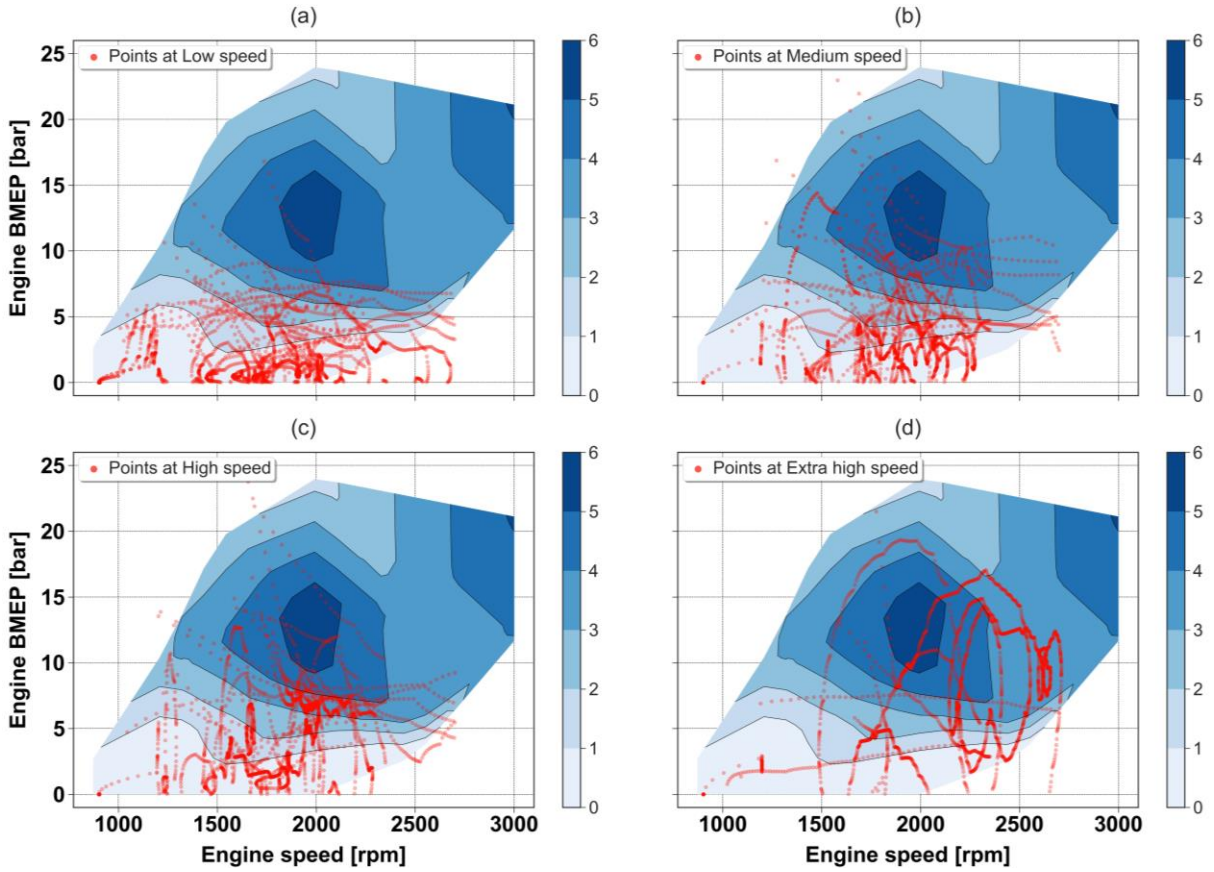

Figure 12. ICE operating points in Case B on the contour map of EGR benefit in fuel consumption, for each WLTP driving cycle part: (a) Low, (b) Medium, (c) High and (d) Extra high. Both axes shared among all plots.

The EGR strategy only leads to a fuel improvement of 1.33% during the urban phase (**Figure 11**), given that the bulk of the engine operation is concentrated at very low loads where the EGR benefit does not exceed 1% (**Figure 12**a). The engine operation is gradually shifted from very low to medium loads as the vehicle speed is increased. Hence the EGR impact on the fuel economy is higher at the medium- and high-speed phases, in which a fuel saving of 2.18% and 2.80% is obtained respectively. At extra-high speeds, most of the ICE operation is located at medium loads and above 2000 rpm, where the EGR benefit is higher than 3% (**Figure 12**d). As noticed in **Figure 11**, the fuel improvement achieved with EGR at the highway part is raised up to 3.34%. After these modeling results, it is concluded that the EGR strategy applied on the SI engine working in the conventional powertrain during a WLTP cycle leads to an overall fuel saving of around 2.6% (27 g), regarding the total fuel consumed without EGR (1052 g).

3.3. Hybrid powertrain optimization

3.3.1. Rule-based EMS calibration

In the rule-based EMS, a series of deterministic rules were defined for the transitions between the different parallel full HEV operation modes, based on the driver power demand, battery SOC and vehicle speed (**Table 4**). Two DOE procedures with 60 simulations each were performed by using the hybrid SUV model, one for the engine operation without EGR and the other one with EGR, to optimize the criteria related to the following variables (DOE factors): upper limit of the vehicle speed (V_{lim}^{up}), hysteresis width (w_h), maximum SOC (SOC_{max}) and width of the SOC interval (w_i). A hysteresis loop was applied on the vehicle speed limit criterion to avoid successive engine starts and shutdowns. Therefore, an upper speed limit was considered to shift from the EV to HEV mode, and a lower speed limit for the opposite transition (**Table 4**). The difference between the upper and lower limits is the hysteresis width. Regarding the width of the SOC interval, it is basically the difference between the maximum and minimum SOC. **Table 6** provides the levels of the DOE factors along with their respective optimum values with and without EGR. Some combinations of SOC_{max} and w_i levels were excluded to guarantee that the battery always operates within the usable SOC window, i.e., between the 30 and 70% SOC [**44**, **45**]. In addition, it was assumed for every simulation that the battery was totally charged at the start.

Table 6. DOE by simulation for the rule-based EMS calibration: factors, levels and optimum values.

DOE factor	Levels	Optimum without EGR	Optimum with EGR
Upper speed limit (km/h)	70, 80 and 90	90	90
Hysteresis width (km/h)	5 and 10	5	5
Maximum SOC (-)	0.55, 0.60, 0.65 and 0.70	0.70	0.70
SOC interval width (-)	0.20, 0.25, 0.30 and 0.40	0.30	0.30

Figure 13 and **Figure 14** show the DOE results in terms of total fuel consumption without and with EGR, respectively. For the sake of a fair fuel consumption comparison, it should be stated that only those simulations in which the final SOC was equal to its initial value were included. Focusing on **Figure 13**a, the fuel consumption for a hysteresis width of 5 km/h is reduced as the upper speed limit is increased. A similar tendency is also observed for a w_h of 10 km/h, although the minimum fuel consumption with a V_{lim}^{up} of 80 km/h is higher than with a V_{lim}^{up} of 70 km/h. In short, the fuel consumption was minimized with an upper speed limit of 90 km/h and a hysteresis width of 5 km/h. Regarding the **Figure 13**b, it is found that increasing the maximum SOC results in a higher fuel economy. The optimum values of SOC_{max} and w_i are equal to 0.7 and 0.3. The same trends as without EGR were observed with EGR (**Figure 14**).

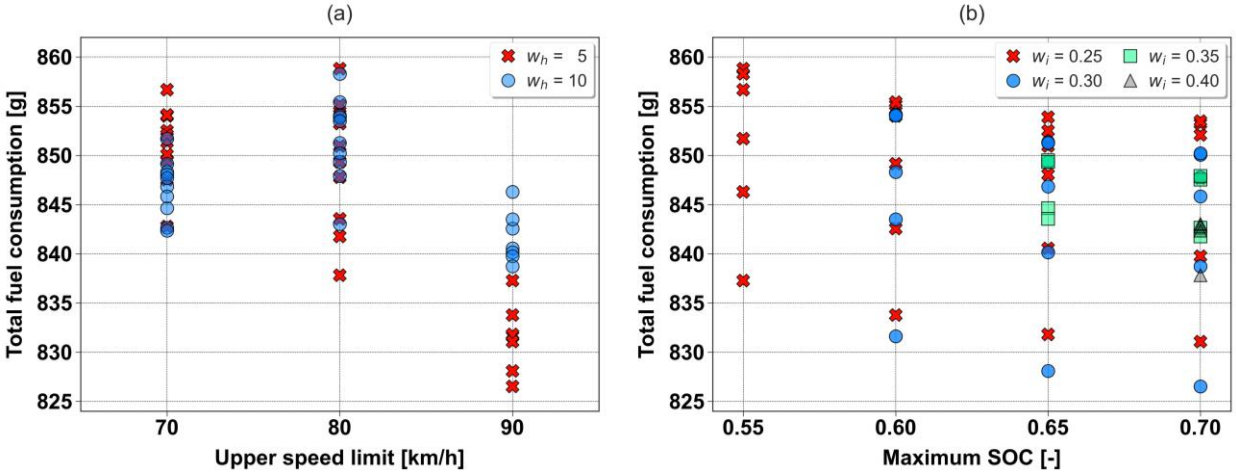

Figure 13. DOE results for the hybrid powertrain without EGR: total ICE fuel consumption versus (a) upper speed limit for different hysteresis widths and versus (b) maximum SOC for different SOC interval widths.

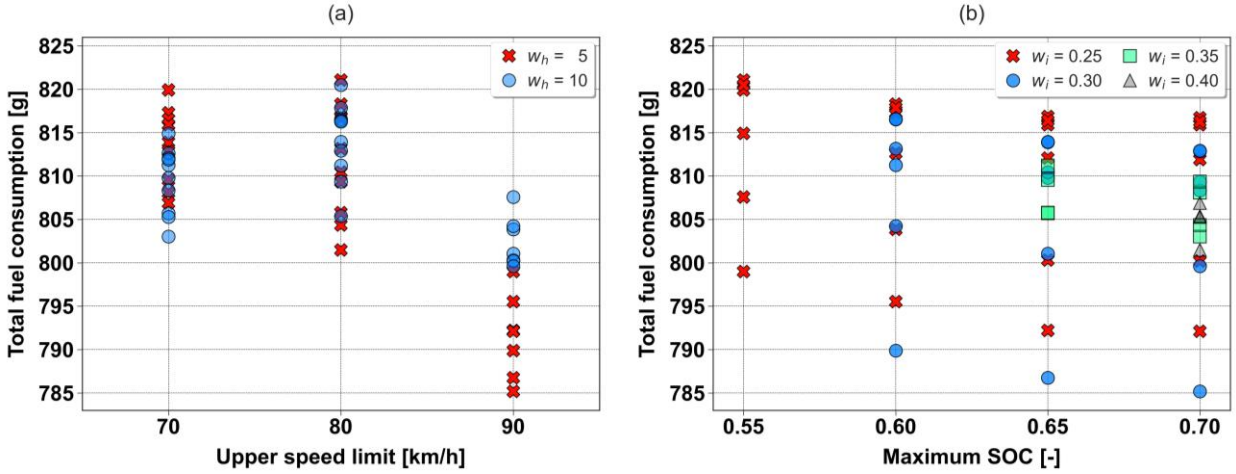

Figure 14. DOE results for the hybrid powertrain with EGR: total ICE fuel consumption versus (a) upper speed limit for different hysteresis widths and versus (b) maximum SOC for different SOC interval widths.

3.3.2. ECMS calibration

Through the ECMS proposed in this research, the ICE torque is optimized at each time step by minimizing the cost function H presented in **Eq.** (7), in which the factors λ and γ are constants to be calibrated. Two values of λ were calculated both with and without EGR, one canceling the third term of **Eq.** (7) associated with the additional fuel consumed during engine

start and warm-up maneuvers ($\gamma = 0$), and the other one considering it ($\gamma \neq 0$). The weighting factor γ was adjusted to reduce the amount of engine starts until reaching the same number of starts as the one obtained in the best case (in terms of fuel consumption) with the rule-based EMS. **Figure 15** depicts the battery SOC (a) and the number of engine start and stop maneuvers (b) during the following three WLTP cycle simulations for the parallel full HEV with no EGR: Case C, the best one with the rule-based EMS; Case D, the one optimized by using the ECMS with $\gamma = 0$; and Case E, the one optimized through the ECMS with $\gamma \neq 0$. Likewise, **Figure 16** illustrates the battery SOC (a) and the number of engine starts and stops (b) for the same three cases as in **Figure 15**, but now with EGR: Case F, G and H, respectively. **Table 7** provides the information needed to identify the two conventional SUV cases (A and B) shown in **Figure 11**, and the six hybrid SUV cases (from C to H) presented in **Figure 15** and **Figure 16**.

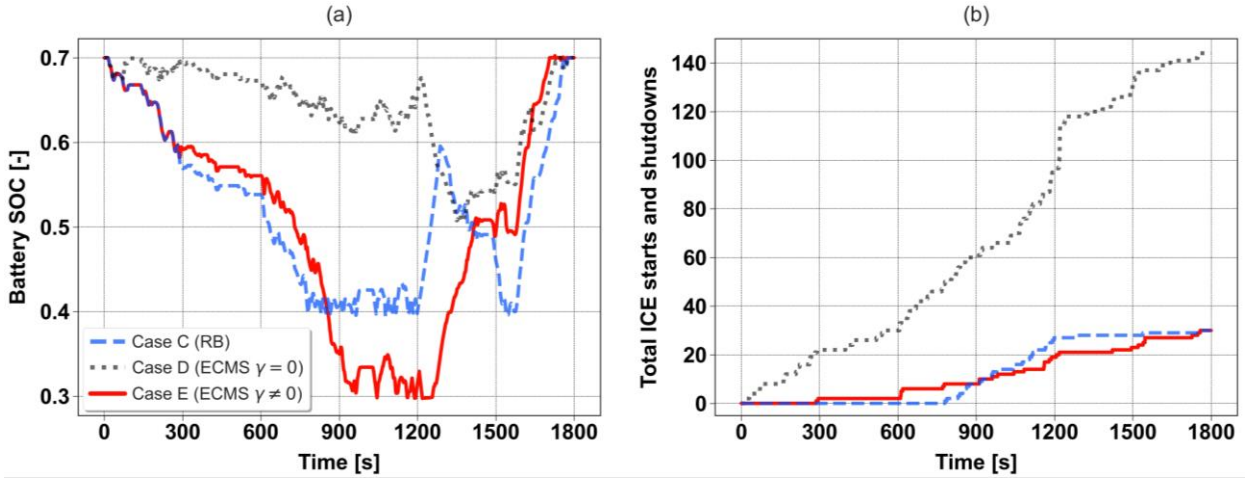

Figure 15. The battery SOC (a) and the total number of engine starts and shutdowns (b) during three WLTP cycle simulations for the parallel FHEV without EGR: Case C (dashed), D (dotted) and E (solid). More details on these cases in **Table 7**.

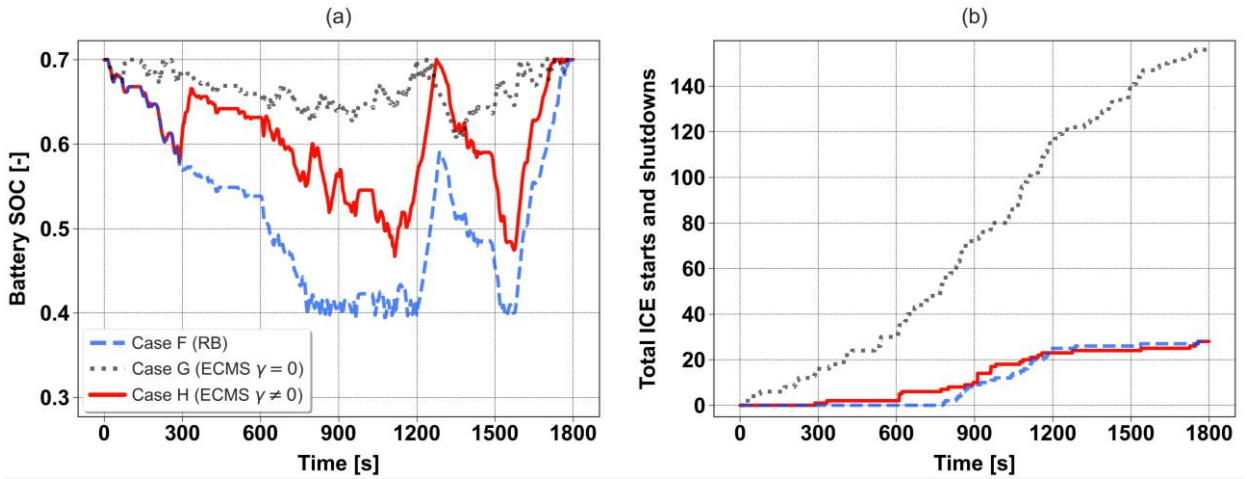

Figure 16. The battery SOC (a) and the total number of engine starts and shutdowns (b) during three WLTP cycle simulations for the parallel FHEV with EGR: Case F (dashed), G (dotted) and H (solid). More details on these cases in **Table 7**.

A constant succession of engine starts and stops was obtained when applying the ECMS with $\gamma = 0$ to manage the energy flows in the hybrid powertrain. More than 70 start maneuvers happen in Case D without EGR (**Figure 15**b) and Case G with EGR (**Figure 16**b). This behavior

is undesirable for many reasons, including drivability issues, fuel economy and emission penalties, and even the deterioration of engine components [**46**, **47**]. Even more, the hypothesis of a quasi-static behavior of the engine used in this study may be unrealistic in the case of frequent starts and stops. The engine starts are significantly reduced in the rule-based EMS cases: 15 without EGR (Case C) and 14 with EGR (Case F). The same numbers of starts were obtained when using the ECMS with $\gamma \neq 0$ in Case E and H. To find the γ values in the latter cases, the total ICE operation time (t_{ICE}) in Case C and F (around 600 s) was used as an input in **Eq.** (10). Regarding the battery SOC, it should be stated that a net battery energy consumption equal to zero was achieved in all cases, as observed in **Figure 15**a and **Figure 16**a. It is also remarkable that hybridization leads to near-zero tailpipe emissions in the urban phase, between 0 and 600 s in the WLTP cycle (**Figure 15**b and **Figure 16**b).

Table 7. Summary of the main characteristics of Case A, B, C, D, E, F, G and H.

Case Name	Powertrain	EGR	EMS	λ (-)	γ (kW)
Case A	Conventional	No	-	-	-
Case B	Conventional	Yes	-	-	-
Case C	Hybrid	No	Rule-based	-	-
Case D	Hybrid	No	Mixed with ECMS	2.7094	0
Case E	Hybrid	No	Mixed with ECMS	2.7047	5.7843
Case F	Hybrid	Yes	Rule-based	-	-
Case G	Hybrid	Yes	Mixed with ECMS	2.5980	0
Case H	Hybrid	Yes	Mixed with ECMS	2.5908	5.3720

3.4. EGR impact on the fuel economy of the hybrid SUV

The bar chart in **Figure 17** depicts the modeled total fuel consumption without EGR for Case A (conventional), C (hybrid with rule-based EMS) and E (hybrid with ECMS), and for their respective counterparts with EGR (Case B, F and H). The modeling results related to the hybrid powertrain optimized through the ECMS with $\gamma = 0$ (Case D and G) were not analyzed in this section due to the issues derived from starting and stopping the engine constantly, as stated in Section 3.3.2. The fuel improvement achieved with EGR for Case B, F and H, compared to their counterparts without EGR, is also included in **Figure 17**, each above its corresponding bar. Besides, **Figure 18** shows the ICE operating points with EGR for Case F during the WLTP cycle simulation, on the contour map of EGR benefit in the fuel consumption. By using the rule-based EMS, the engine operation without (Case C) and with EGR (Case F) is very similar. In both cases, the ICE operates on the minimum BSFC curve mostly between 1750 and 2250 rpm, where the EGR benefit in fuel economy is maximum (4-6%). This is clearly reflected in the total fuel consumption (**Figure 17**), leading to a saving of 5% comparing Case C (826 grams of fuel) and Case F (784 g). This saving is almost twice the one obtained because of the EGR strategy for the conventional SUV (2.6%).

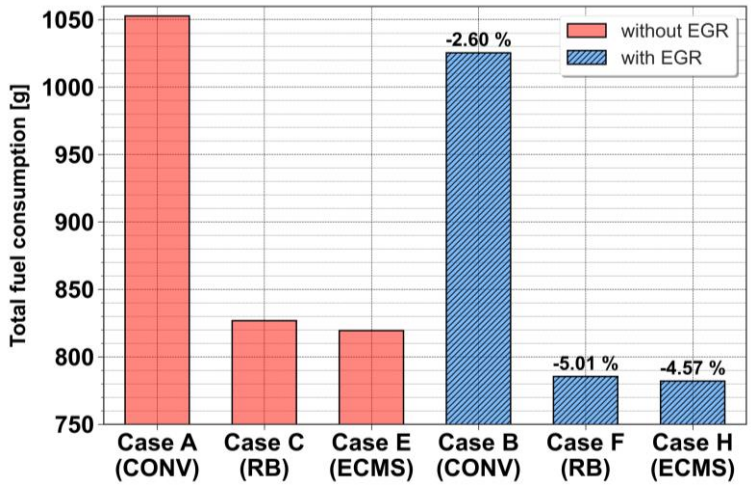

Figure 17. Modeled total fuel consumption without EGR for Case A (conventional), C (rule-based EMS) and E (ECMS with $\gamma \neq 0$), and for their respective counterparts with EGR (Case B, F and H).

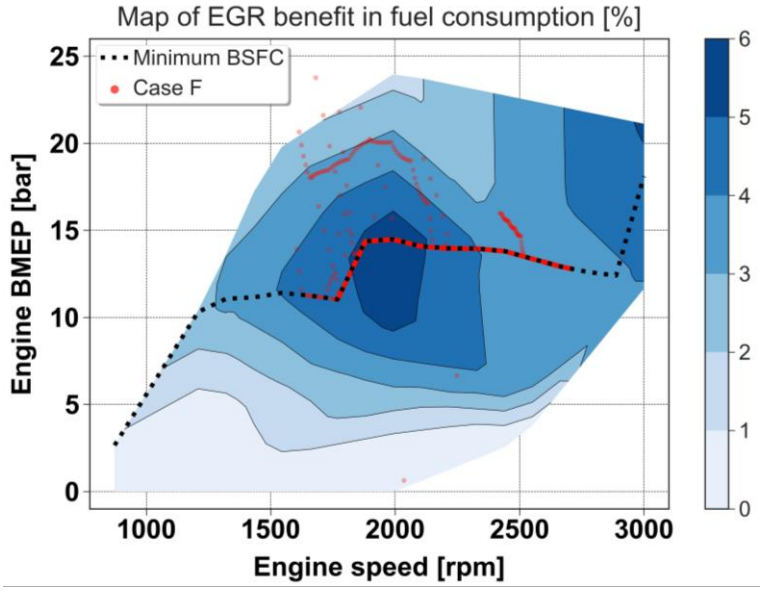

Figure 18. ICE operating points on the contour map of EGR benefit in fuel consumption during the WLTP cycle simulation for Case F.

Figure 19 depicts the engine operating points for Case E (a) and Case H (b) during the WLTP cycle simulation, on the BSFC contour map without and with EGR. Through the mixed EMS with ECMS ($\gamma \neq 0$), the engine operation is not fully concentrated on the minimum BSFC curve, unlike in the cases with the rule-based EMS. The engine performance for Case E and H is comparable and it can be divided into three ICE speed zones:

- The engine generally operates around the minimum BSFC curve below 1750 rpm.
- Between 1750 and 2100 rpm, the load of the operating points is mainly lower than the minimum BSFC torque (**Figure 19**), although most of such points are maintained within the same BSFC zone (around 240 g/kWh).
- Above 2100 rpm, the engine works just inside the minimum BSFC area (**Figure 19**). The operation time in this area for Case E and H (around 250 s) is 25% higher than for Case C and F with the rule-based EMS (around 200 s). The latter is required to compensate the lower

power delivered by the engine between 1750 and 2100 rpm, with the aim of achieving zero net battery energy consumption.

Because of the increased engine power delivered at the minimum BSFC area, the ECMS with $\gamma \neq 0$ (constrained by a rule-based control) provides a better fuel economy than the rule-based EMS, while the drivability is quite similar through both energy management strategies. More specifically, the fuel consumption without EGR in Case E (ECMS) is 1.0% lower than in Case C (rule-based EMS). Focusing on the EGR benefit, a fuel improvement of 4.6% is achieved with EGR comparing Case E (819 grams of fuel) and Case H (782 g), when using the mixed EMS with ECMS. This fuel saving is slightly lower than the 5% obtained through the rule-based EMS by comparing Case C and F. The explanation to the latter is the increase in the engine operation time at the minimum BSFC zone (around 2400 rpm) in the cases with ECMS, while the EGR benefit is maximum between 1750 and 2100 rpm (**Figure 18**).

It should be also stated that the powertrain hybridization results in a fuel consumption reduction higher than 22%, comparing the performances of the parallel full HEV and its conventional counterpart during the homologation cycle. In particular, fuel savings of 22.1%, comparing the cases without EGR (Case A vs. E), and 23.7%, comparing the cases with EGR (Case B vs. H), were achieved because of hybridization. These values of fuel improvement are in the same order of magnitude as the ones reported in other two comparable research studies [**7**, **10**], in which a parallel full HEV with a gasoline engine and its conventional counterpart are also simulated under WLTP driving cycle conditions.

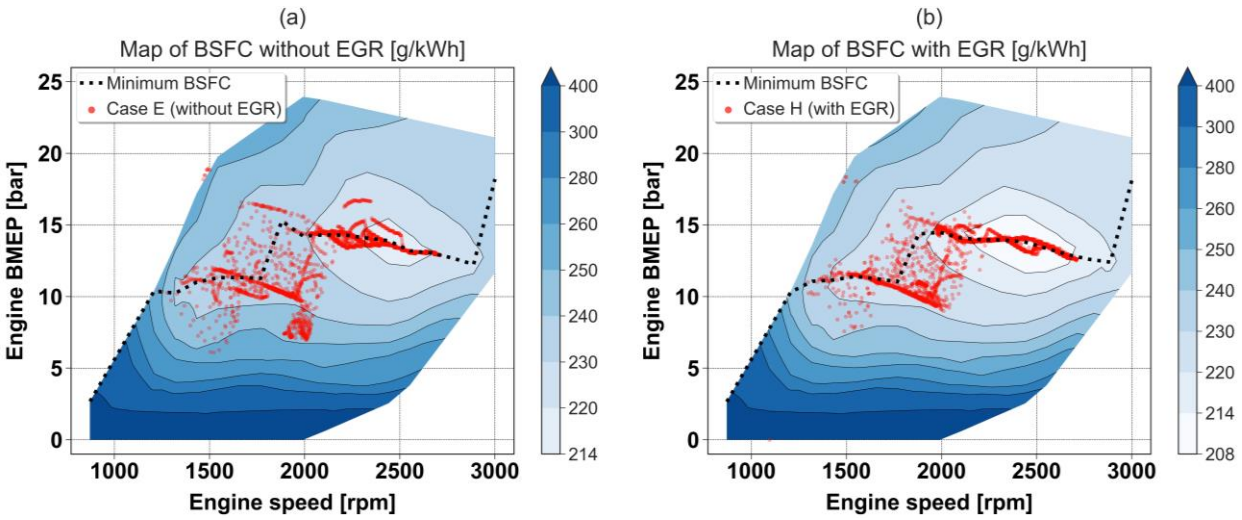

Figure 19. ICE operating points during the WLTP cycle simulation for Case E (a) and Case H (b), on the BSFC contour map without and with EGR respectively.

4. Summary and conclusions

This research aimed to evaluate by simulation the fuel consumption reduction achieved when applying the EGR strategy on advanced SI engines, working in both conventional and hybrid-electric powertrains under driving cycle conditions. For that purpose, the 0D models of a parallel full hybrid SUV and its conventional counterpart were built in GT-Power. These models were fed with the experimental fuel consumption and emission maps of a SI gasoline engine operating with and without EGR. In the interest of reliability, the transient performance of the conventional SUV model was validated in terms of fuel consumption, by using the experimental data of a WLTP class 3b driving cycle performed in the engine test cell.

Firstly, two WLTP homologation cycles were simulated by means of the conventional SUV model: one considering an engine operation without EGR and the other with EGR. It was found that the EGR strategy leads to a fuel improvement of 2.6% for conventional cars during the WLTP cycle. After that, hybrid SUV simulations were also done. Two energy management strategies (EMS) were applied in this study: a deterministic rule-based EMS and an equivalent consumption minimization strategy (ECMS). The proposed ECMS optimized the power split between the engine and electric motor based on the fuel economy and drivability. Modeling results revealed that the powertrain hybridization results in a fuel saving higher than 22%, comparing the performances of the parallel full HEV and its conventional counterpart during the WLTP homologation cycle. Besides, hybridization led to near-zero tailpipe emissions in the WLTP urban phase.

Regarding the EGR strategy, it should be remarked that the powertrain hybridization enables to shift the engine operation from low to medium loads, where the EGR benefit in the fuel economy is just maximum, so a further fuel saving was expected. EGR resulted in a fuel improvement of 4.6% for the hybrid powertrain during the WLTP cycle, 2% more than for the conventional one. Therefore, the hybrid SUV simulations confirmed that hybridization benefits the application of EGR strategy on advanced SI gasoline engines, providing an additional fuel saving.

References

1. European Commission: DG Climate Action. "Communication from the Commission to the European Parliament, the Council, the European Economic and Social Committee and the Committee of the Regions: Stepping up Europe's 2030 climate ambition. Investing in a climate-neutral future for the benefit of our people", Brussels, 2020.

2. Gröger, O., Gasteiger, H. A., Suchsland, J.-P. "Review— Electromobility: Batteries or Fuel Cells? ". *Journal of the Electrochemical Society*, 162, A2605–A2622, 2015. https://doi.org/10.1149/2.0211514jes

3. Qiao, Q., Zhao, F., Liu, Z., Jiang, S., Hao, H. "Comparative study on life cycle CO2 emissions from the production of electric and conventional vehicles in China". *EnergyProcedia*, 105, 3584, 2017. https://doi.org/10.1016/j.egypro.2017.03.827

4. Anselma, P. G., Biswas, A., Belingardi, G., Emadi, A. "Rapid assessment of the fuel economy capability of parallel and series-parallel hybrid electric vehicles". *Applied Energy*, 275, 115319, 2020. https://doi.org/10.1016/j.apenergy.2020.115319

5. Luján, J. M., Garcia, A., Monsalve-Serrano, J., Martínez-Boggio, S. "Effectiveness of hybrid powertrains to reduce the fuel consumption and NOx emissions of a Euro 6d-temp diesel engine under real-life driving conditions". *Energy Conversion and Management*, 199, 111987, 2019. https://doi.org/10.1016/j.enconman.2019.111987

6. Asghar, M., Bhatti, A. I., Ahmed, Q., Murtaza, G. "Energy management strategy for Atkinson cycle engine based parallel hybrid electric vehicle". *IEEE Access*, 6, 28008-28018, 2018. https://doi.org/10.1109/ACCESS.2018.2835395

7. García, A., Monsalve-Serrano, J., Martínez-Boggio, S., Wittek, K. "Potential of hybrid powertrains in a variable compression ratio downsized turbocharged VVA Spark Ignition engine". *Energy*, 195, 117039, 2020. https://doi.org/10.1016/j.energy.2020.117039

8. Huang, Y., Surawski, N. C., Organ, B., Zhou, J. L., Tang, O. H., Chan, E. F. C. "Fuel consumption and emissions performance under real driving: Comparison between hybrid and conventional vehicles". *Science of the Total Environment*, 659, 275-282, 2019. https://doi.org/10.1016/j.scitotenv.2018.12.349

9. Lemazurier, L., Shidore, N., Kim, N., Moawad, A., Rousseau, A., Bonkoski, P., Delhom, J. "Impact of Advanced Engine and Powertrain Technologies on Engine Operation and Fuel Consumption for Future Vehicles". SAE Technical Paper 2015-01-0978, 2015. https://doi.org/10.4271/2015-01-0978

10. Conway, G., Chambon, P., Alger, T. "Opportunities for Electrified Internal Combustion Engines". SAE Technical Paper 2020-01-0281, 2020, https://doi.org/10.4271/2020-01-0281

11. Soleimani, M., Campean, F., Neagu, D. "Reliability challenges for automotive aftertreatment systems: a state-of-the-art perspective". *Procedia Manufacturing*, 16, 75-82, 2018. https://doi.org/10.1016/j.promfg.2018.10.174

12. Fraser, N., Blaxill, H., Lumsden, G., Bassett, M. "Challenges for Increased Efficiency through Gasoline Engine Downsizing". *SAE Int J Engines*, 2, 991-1008, 2009. https://doi.org/10.4271/2009-01-1053

13. Coltman, D., Turner, J. W. G., Curtis, R., Blake, D., Holland, B., Pearson, R. J., Arden, A., Nuglisch, H. "Project Sabre: A Close-Spaced Direct Injection 3-Cylinder Engine with Synergistic Technologies to Achieve Low CO2 Output". *SAE Int J Engines*, 1, 129-146, 2009. https://doi.org/10.4271/2008-01-0138

14. Lumsden, G., OudeNijeweme, D., Fraser, N., Blaxill, H. "Development of a Turbocharged Direct Injection Downsizing Demonstrator Engine". *SAE Int J Engines*, 2, 1420-1432, 2009. https://doi.org/10.4271/2009-01-1503

15. Shahed, S. and Bauer, K. "Parametric Studies of the Impact of Turbocharging on Gasoline Engine Downsizing". *SAE Int. J. Engines*, 2, 1347-1358, 2009. https://doi.org/10.4271/2009-01-1472

16. Takaki, D., Tsuchida, H., Kobara, T., Akagi, M., Tsuyuki, T., Nagamine, M. "Study of an EGR System for Downsizing Turbocharged Gasoline Engine to Improve Fuel Economy". SAE Technical Paper 2014-01-1199, 2014. https://doi.org/10.4271/2014-01-1199

17. Alger, T., Chauvet, T., Dimitrova, Z. "Synergies between High EGR Operation and GDI Systems". *SAE Int. J. Engines*, 1, 101-114, 2009. https://doi.org/10.4271/2008-01-0134

18. Luján, J. M., Climent, H., Novella, R., Rivas-Perea, M. E. "Influence of a low pressure EGR loop on a gasoline turbocharged direct injection engine". *Applied Thermal Engineering*, 89, 432-443, 2015. https://doi.org/10.1016/j.applthermaleng.2015.06.039

19. Siokos, K., Koli, R., Prucka, R., Schwanke, J., Miersch, J., "Assessment of Cooled Low Pressure EGR in a Turbocharged Direct Injection Gasoline Engine", *SAE Int. J. Engines*, 8, 1535-1543, 2015. https://doi.org/10.4271/2015-01-1253

20. Potteau, S., Lutz, P., Leroux, S., Moroz, S., Tomas, E. "Cooled EGR for a Turbo SI Engine to Reduce Knocking and Fuel Consumption". SAE Technical Paper 2007-01-3978, 2007. https://doi.org/10.4271/2007-01-3978

21. Chan, C. C., Bouscayrol, A., Chen, K. "Electric, hybrid, and fuel-cell vehicles: Architectures and modeling". *IEEE transactions on vehicular technology*, 59, 589-598, 2009. https://doi.org/10.1109/TVT.2009.2033605

22. Benajes, J., Garcia, A., Monsalve-Serrano, J., Martinez-Boggio, S. "Emissions reduction from passenger cars with RCCI plug-in hybrid electric vehicle technology". *Applied Thermal Engineering*, 164, 114430, 2020. https://doi.org/10.1016/j.applthermaleng.2019.114430

23. European Automobile Manufacturers' Association. "Fuel types of new cars: battery electric 9.8%, hybrid 20.7% and petrol 39.5% market share in Q3 2021". Brussels, October 22, 2021 (accessed on December 12, 2021). https://www.acea.auto/fuel-pc/fuel-types-of-new-cars-battery-electric-9-8-hybrid-20-7-and-petrol-39-5-market-share-in-q3-2021/

24. Zhuang, W., Li, S., Zhang, X., Kum, D., Song, Z., Yin, G., Ju, F. "A survey of powertrain configuration studies on hybrid electric vehicles". *Applied Energy*, 262, 114553, 2020. https://doi.org/10.1016/j.apenergy.2020.114553

25. Galindo, J., Climent, H., de la Morena, J., González-Domínguez, D., Guilain, S., Besançon, T. "Assessment of air-management strategies to improve the transient performance of a gasoline engine under high EGR conditions during load-decrease operation". *International Journal of Engine Research*, 2021. https://doi.org/10.1177/14680874211055578

26. Payri F., Lujan J., Climent H., Pla B. "Effects of the Intake Charge Distribution in HSDI Engines". SAE Technical Paper 2010-01-1119, 2010. https://doi.org/10.4271/2010-01-1119

27. Pla, B., De La Morena, J., Bares, P., Jiménez, I. "Knock Analysis in the Crank Angle Domain for Low-Knocking Cycles Detection". SAE Technical Paper 2020-01-0549, 2020. https://doi.org/10.4271/2020-01-0549

28. Pla, B., De la Morena, J., Bares, P., Jiménez, I. "Cycle-to-cycle combustion variability modelling in spark ignited engines for control purposes". *International Journal of Engine Research*, 21, 1398-1411, 2020. https://doi.org/10.1177/1468087419885754

29. Serrano, J., Climent, H., Navarro, R., González-Domínguez, D. "Methodology to Standardize and Improve the Calibration Process of a 1D Model of a GTDI Engine". SAE Technical Paper 2020-01-1008, 2020. https://doi.org/10.4271/2020-01-1008

30. Galindo, J., Climent, H., De la Morena, J., González-Domínguez, D., Guilain, S., Besançon, T. "Experimental and modeling analysis on the optimization of combined VVT and EGR strategies in turbocharged direct-injection gasoline engines with VNT". *Proceedings of the Institution of Mechanical Engineers, Part D: Journal of Automobile Engineering*, 235, 2843-2856, 2021. https://doi.org/10.1177/09544070211004502

31. Serrano, J. R., Arnau, F. J., García-Cuevas, L. M., Gómez-Vilanova, A., Guilain, S., Batard, S. "A Methodology for Measuring Turbocharger Adiabatic Maps in a Gas-Stand and Its Usage for Calibrating Control Oriented and One-Dimensional Models at Early ICE Design Stages". *ASME. J. Energy Resour. Technol*., 143, 042303, 2021. https://doi.org/10.1115/1.4048229

32. Ghojel, J. I. "Review of the development and applications of the Wiebe function: A tribute to the contribution of Ivan Wiebe to engine research". *International Journal of Engine Research*, 11, 297-312, 2010. https://doi.org/10.1243/14680874JER06510

33. Lavoie, G.A., Ortiz-Soto, E., Babajimopoulos, A., Martz, J.B., Assanis, D.N. "Thermodynamic sweet spot for high-efficiency, dilute, boosted gasoline engines". *International Journal of Engine Research*, 14, 260-278, 2013. https://doi.org/10.1177/1468087412455372

34. Gamma Technologies LLC. "Vehicle Driveline and HEV Application Manual". Westmont, USA, 2018.

35. Onori, S., Serrao, L., Rizzoni, G. "Hybrid electric vehicles: Energy management strategies". London, UK: Springer, 2016. https://doi.org/10.1007/978-1-4471-6781-5

36. Zhang, F., Wang, L., Coskun, S., Pang, H., Cui, Y., Xi, J. "Energy management strategies for hybrid electric vehicles: Review, classification, comparison, and outlook". *Energies*, 13, 3352, 2020. https://doi.org/10.3390/en13133352

37. Panday, A., Bansal, H. O. "A review of optimal energy management strategies for hybrid electric vehicle". *International Journal of Vehicular Technology*, 2014, 1-19, 2014. https://doi.org/10.1155/2014/160510

38. Paganelli, G., Ercole, G., Brahma, A., Guezennec, Y., Rizzoni, G. "General supervisory control policy for the energy optimization of charge-sustaining hybrid electric vehicles". *JSAE review*, 22, 511-518, 2001. https://doi.org/10.1016/S0389-4304(01)00138-2

39. Sciarretta, A., Back, M., Guzzella, L. "Optimal control of parallel hybrid electric vehicles". *IEEE Transactions on control systems technology*, 12, 352-363, 2004. https://doi.org/10.1109/TCST.2004.824312

40. Sun, C., He, H., Sun, F. "The role of velocity forecasting in adaptive-ECMS for hybrid electric vehicles". *Energy Procedia*, 75, 1907-1912, 2015. https://doi.org/10.1016/j.egypro.2015.07.181

41. Climent, H., Pla, B., Bares, P., Pandey, V. "Exploiting driving history for optimising the Energy Management in plug-in Hybrid Electric Vehicles". *Energy Conversion and Management*, 234, 113919, 2021. https://doi.org/10.1016/j.enconman.2021.113919

42. Škugor, B., Deur, J., Cipek, M., Pavković, D. "Design of a power-split hybrid electric vehicle control system utilizing a rule-based controller and an equivalent consumption minimization strategy". *Proceedings of the Institution of Mechanical Engineers, Part D: Journal of Automobile Engineering*, 228, 631-648, 2014. https://doi.org/10.1177/0954407013517220

43. Rezaei, A., Burl, J. B., Zhou, B. "Estimation of the ECMS equivalent factor bounds for hybrid electric vehicles". *IEEE Transactions on Control Systems Technology*, 26, 2198-2205, 2017. https://doi.org/10.1109/TCST.2017.2740836

44. Benajes, J., Garcia, A., Monsalve-Serrano, J., Martínez-Boggio, S. "Optimization of the parallel and mild hybrid vehicle platforms operating under conventional and advanced combustion modes". *Energy Conversion and Management*, 190, 73-90, 2019. https://doi.org/10.1016/j.enconman.2019.04.010

45. Pesaran, A. A., Markel, T., Tataria, H. S., Howell, D. "Battery requirements for plug-in hybrid electric vehicles--Analysis and rationale". Conference paper NREL/CP-540-42240, in the 23rd International Electric Vehicle Symposium (EVS-23), Anaheim, California (United States of America), 2007. https://www.osti.gov/servlets/purl/923227

46. Opila, D. F., Wang, X., McGee, R., Gillespie, R. B., Cook, J. A., Grizzle, J. W. "An energy management controller to optimally trade off fuel economy and drivability for hybrid vehicles". *IEEE Transactions on Control Systems Technology*, 20(6), 1490-1505, 2011. https://doi.org/10.1109/TCST.2011.2168820

47. Wei, X. "Modeling and control of a hybrid electric drivetrain for optimum fuel economy, performance and driveability". Doctoral dissertation, The Ohio State University, Ohio, USA, 2004. Retrieved from http://rave.ohiolink.edu/etdc/view?acc_num=osu1095960915